Estimation of the total sub-debris ablation from point-scale ablation data on a debris-covered glacier

Sunil S Singh[1] , Argha Banerjee[2], Harish C Nainwal[1], R Shankar[3]

[1]Department of Geology, HNB Garhwal university, Srinagar, Uttarakhand, India
[2]Earth and Climate Science, Indian Institute of Science Education and Research, Pune, India
[3]The Institute of Mathematical Sciences, Chennai, India

Correspondence: Argha Banerjee <argha@iiserpune.ac.in>

Estimation of the total sub-debris ablation from point-scale ablation data on a debris-covered glacier

Sunil S. Singh,[1] Argha Banerjee,[2] Harish C. Nainwal,[1] R. Shankar[3]

[1]*Department of Geology, HNB Garhwal university, Srinagar, Uttarakhand, India*

[2]*Earth and Climate Science, Indian Institute of Science Education and Research, Pune, India*

[3]*The Institute of Mathematical Sciences, Chennai, India*

Correspondence: Argha Banerjee <argha@iiserpune.ac.in>

ABSTRACT. Glaciological mass balance is computed from point-scale field data at a few ablation stakes that are regressed as a function of elevation, and averaged over the area-elevation distribution of the glacier. This method is contingent on a tight control of elevation on local ablation. On debris-covered glaciers, systematic and random spatial variations of debris thickness modify ablation rates. A method that takes into account the debris-thickness variability in extrapolating point-scale ablation data may be more accurate on these glaciers. We propose and test a method where stake data are interpolated as a function of debris-thickness alone, and averaged over the observed debris-thickness distribution at different parts of the glacier. We apply this method to compute sub-debris ablation rate on Satopanth Glacier (Central Himalaya) utilising about a thousand ablation measurements at a network of up to 56 stakes during 2015–2017. We compare our results with that from the standard glaciological method. The uncertainties in both the estimates due to the corresponding uncertainties in measurement of ablation and debris-thickness distribution, and that due to interpolation procedures are estimated using Monte Carlo methods. Possible biases due to finite number of stakes used are investigated, and net specific balance of Satopanth glacier is computed.

1. INTRODUCTION

Extensive supraglacial debris mantle on the ablation zone can modify glacier response to climate forcing (Scherler and others, 2011; Gardelle and others, 2013; Nuimura and others, 2012; Banerjee and Shankar, 2013; Brun and others, 2017; King and others, 2018). The supraglacial debris layer mediates the melt-energy supply to ice-surface underneath. A thick debris layer inhibits melt by insulating the ice, whereas a thin-debris layer increases melt due to a lower albedo (Østrem, 1959; Collier and others, 2014). However, in the limit of a very thin debris layer ($\lesssim 2$cm), increased evaporation reduces energy available for melting (Collier and others, 2014) leading to a decline in ablation (Østrem, 1959). Supraglacial debris advects with the ice flow, and the debris layer generally thickens downglacier as the ice velocity declines (Benn and Lehmkuhl, 2000; Kirkbride and Deline, 2013; Anderson and Anderson, 2016). This thickening of debris layer causes a systematic reduction in ablation rate down-glacier, even as elevation decreases. This is in contrast with the monotonic increase in ablation downglacier that is usually observed in debris-free glaciers (Oerlemans, 2001). The resultant inverted mass-balance profile on the debris-covered ablation zone has profound implications on the evolution of a glacier under a warming climate (Banerjee and Shankar, 2013). The most striking feature of which is a decoupling of length and mass changes of the glacier right after the warming starts: A thickly debris-covered glacier initially loses mass mostly by thinning, even as its length remain steady over a period of stagnation that may span several decades (Naito and others, 2000; Banerjee and Shankar, 2013). A combination of slow evolution of the ice-flux patterns under the climate forcing and low melt rates beneath the debris cover are responsible for the formation of the stagnant tongue. Beyond this the period of stagnation, a relatively high net mass-loss rate is expected on debris-covered glaciers (Banerjee, 2017). With extensive supraglacial debris cover over 40% of the total ice mass in the ablation zones of several regions in the Himalaya-Karakoram (Kraaijenbrink and others, 2017), the above-mentioned debris-effects have left strong imprints in the recent ice-loss pattern at the third pole (Scherler and others, 2011; Gardelle and others, 2013; Nuimura and others, 2012; Banerjee and Shankar, 2013; Brun and others, 2017; King and others, 2018) and may crucially impact its future evolution as well (Kraaijenbrink and others, 2017).

The smooth down-glacier increase in debris thickness, and corresponding decline of the surface ablation rate as discussed above, provide only a first order description of the debris-effect (Benn and Lehmkuhl, 2000; Scherler and others, 2011a; Banerjee and Shankar, 2013). The role of several other complicating factors, e.g., the presence of numerous thermokarst ephemeral ponds and cliffs that increase local melt-rate
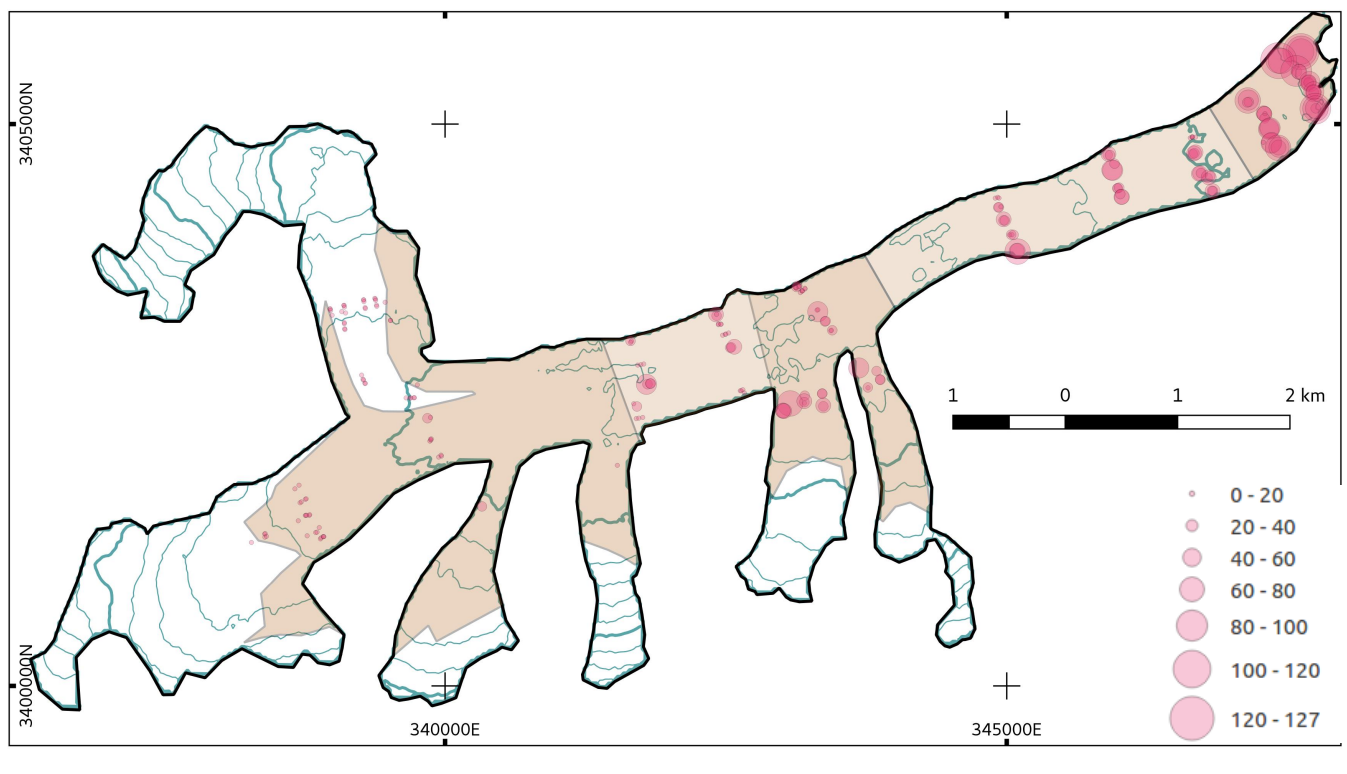
Fig. 1. A map of Satopanth Glacier (30.73N, 79.32E; the central Himalaya) showing the glacier boundary (thick black line), debris extent (shaded areas), and location of ablation stakes (filled circles). The size of the circles denote the debris thickness value (in cm). The debris-covered area is partitioned into five different that are shown here (see text for details). 100m surface elevation contours are plotted with thin blue lines, with thicker lines highlighting 4000, 4500, 5000, 5500, and 6000 m contour lines.

56 (Reynolds, 2000; Sakai and others, 2000; Miles and others, 1993), vertical and horizontal variation of the

57 thermal properties of debris (Nicholson and Benn, 2013; Rowan and others, 2018), random short-scale

58 spatial variation of debris thickness (Mihalcea and others, 2006; Zhang and others, 2011; Nicholson and

59 Mertes, 2017; Rounce and others, 2018), and the accumulation contribution from avalanches (Laha and

60 others, 2017) need to be quantified for accurate surface mass-balance estimates on any typical debris-covered

61 Himalayan glacier. The standard glaciological mass-balance measurement protocol (Kaser and others, 2003)

62 may not be designed to handle some of the above issues. Among the complications listed above, random

63 spatial fluctuation of supraglacial debris thickness, and its implication on glacier mass balance have been

64 highlighted only recently (Nicholson and others, 2018). The ablation rate variability due to the spatially

65 fluctuating debris thickness is likely to be a significant limiting factor for the accuracy of glaciological mass-

66 balance measurements on debris-covered glaciers, as estimation of glacier-wide mean specific ablation from

67 observation at a finite set of stakes assumes that ablation rate is determined solely by elevation (Cogley,

68 1999).

69 In this paper, field data from debris-covered Satopanth Glacier (Central Himalaya, India) are used to

70 investigate the effects of spatial fluctuation of debris thickness on the accuracy of glaciological mass-balance

71 estimates. A possible alternative protocol for mass-balance estimation over the debris-covered ablation

72 zone is proposed and tested. We analyse 1,100 approximately bi-weekly measurements of ablation rate at a

73 network of up to 56 bamboo stakes over the ablation seasons of 2015, 2016, and 2017. Debris-thickness data

74 from 191 pits dug on glacier surface are used to study the debris-thickness distribution. We interpolate

75 the observed point-scale ablation rates as a function of I) elevation, and II) debris thickness at the stakes.

76 The interpolated values for each of the measurement periods were then averaged over glacier hypsometry

77 (method-I, the standard glaciological method) and the zonal debris-thickness distribution (method-II),

78 respectively, to obtain two estimates of the total ablation over the debris-covered area. The reliability of

79 both the regression methods are quantified, the estimated mean sub-debris ablation obtained from both

80 the methods are compared, and uncertainties in the estimates are analysed. Possible biases in the ablation

81 estimates as a function of the number of stakes used are investigated for the two methods.

2. GLACIOLOGICAL MASS BALANCE MEASUREMENT AND DEBRIS COVER

83 Glaciological mass balance estimation is one of the most basic and fundamental tools in glaciology. This

84 relatively simple and robust method estimates the mean specific mass balance of a glacier using observations

85 of ablation rates at a network of relatively small ($\sim 5 - 15$) number of stakes (Fountain and Vecchia, 1999;

86 Kaser and others, 2003). In one of precribed procedure (Kaser and others, 2003), the stake data are fitted

87 to a quadratic curve as function of elevation, and then averaged over the corresponding area-elevation

88 distribution (Kaser and others, 2003) to obtain total (or mean) ablation. Interestingly, the number of

89 stakes required is largely independent of the size of the glacier as long as its area is $\lesssim 10$ km^2 (Fountain

90 and Vecchia, 1999). The robustness of the method relies upon strongly correlated surface ablation rates at

91 locations within the same elevation band (Cogley, 1999). An alternative procedure (Kaser and others, 2003)

92 involves preparing a contour-map of net mass balance based on the stake data. Here, detailed knowledge

93 of local field conditions could be incorporated to improve the accuracy of the estimate.

94 The presence of extensive supraglacial debris cover poses several problems for the above glaciological

95 mass-balance estimation method so that the standard mass-balance manual (Kaser and others, 2003)

96 advises against choosing debris-covered glacier for glaciological mass-balance measurements: "It is most

convenient if the glacier is free of debris cover. A debris cover, usually limited to the tongues, complicates

the interpretation of the climate- glacier interaction. Besides of this theoretical consideration the installation

and maintenance of an ablation network (stakes) is difficult. Even if it was installed, the regular visits to such

a stake in the middle of more or less loose boulders of each size is dangerous" (Kaser and others, 2003). Apart

from these practical considerations, a major issue with the standard glaciological method is that it does

not take into account the random spatial variability of debris thickness. While supraglacial debris thickness

increases systematically downglacier and thus, may be correlated with elevation on glaciers with simple

geometry (Anderson and Anderson, 2016), a relatively large local variability of debris thickness is known

to be present at any given elevation band (Nicholson and others, 2018). This random variability of debris

thickness would lead to a corresponding large variability in the ablation rate within each elevation band,

so that data from an individual stake may not represent the total ablation in the corresponding elevation

band. Moreover, because of the non-linear dependence of ablation rate on debris-thickness (Østrem, 1959),

mean debris thickness in a elevation band can not be used to estimate mean melt rate (Nicholson and

others, 2018). The contour map based extrapolation of stake data can be more accurate as field knowledge

of large-scale debris-thickness variation may be incorporated into the calculation. However, the local-scale

debris thickness variability discussed above would still be an issue.

For a rough estimate of the magnitude of the effects of debris variability on ablation rate, let us assume

the following form for the variation of ablation rate b with debris thickness d (Evatt and others, 2013;

Anderson and Anderson, 2016),

$$b(d) = \frac{b_0}{1 + d/d_0} \,. \tag{1}$$

Here, b_0 is the ablation rate on debris-free ice, and d_0 (~ 10 cm) is a characteristic debris-thickness scale

(Anderson and Anderson, 2016). The above formula implies that a possible variation of debris thickness

from, say about 10 cm to 1 m can reduce the ablation rate by a factor of about 6. Similar variation in

ablation rate for clean ice Himalayan glaciers with typical mass balance gradients (~ 0.6 m w.e. yr^{-1}

100 m^{-1}) would correspond to an elevation change of about a thousand meters (Azam and others, 2018).

Therefore, on a debris-covered glacier both the systematic variation of debris thickness along the length

of the glacier, and its large-amplitude short-scale spatial fluctuations (Nicholson and others, 2018), can

potentially mask the elevation dependence of mass balance. The systematic down-glacier variation of mean

debris thickness may be correlated with elevation, and usually leads to an inverted mass-balance gradient

125 in debris-covered glaciers (Benn and Lehmkuhl, 2000). However, the accuracy of the standard glaciological

126 method that uses elevation-dependent regression curve may be quite susceptible to the effects of random

127 short-scale large-amplitude spatial variability of the debris thickness. These random local fluctuations

128 in debris thickness may have to be characterised, and taken into account while interpolating the point

129 measurements at stakes over the total debris-covered ablation zone. Otherwise, biases may be introduced

       in the interpolated ablation estimates (Nicholson and others, 2018).
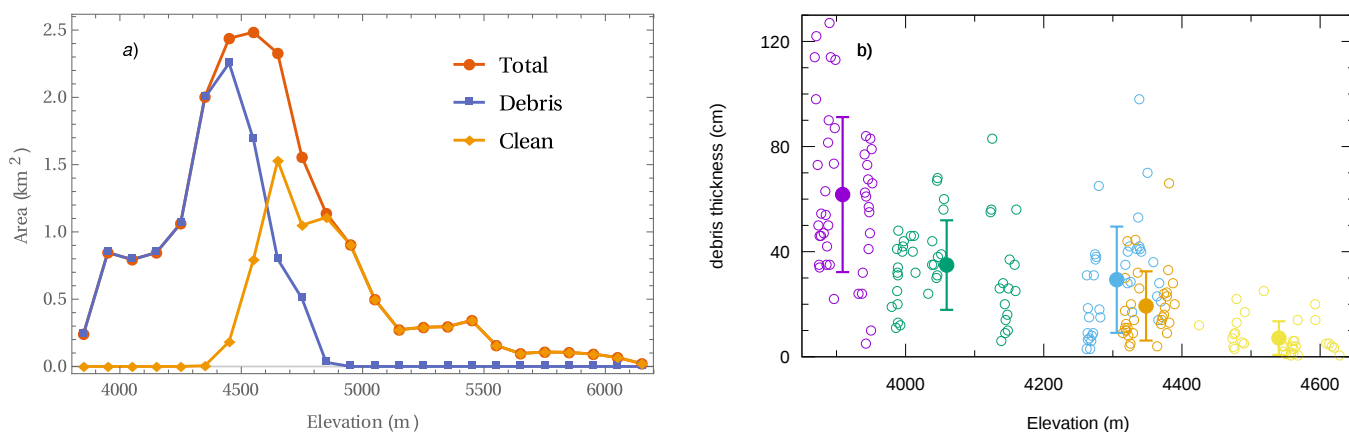
Fig. 2. (a) Area-elevation distribution of clean-ice area, debris-covered area and glacier area, with elevation binsize of
100 m. (b) Variation of debris thickness on Satopanth Glacier. Different symbol colour represents subzones marked in
Fig.1, with open symbols representing individual measurement of debris thickness. The mean and standard deviation
of the debris thickness in each zone is shown solid symbol with bars.

130

3. STUDY AREA

131

132 Satopanth Glacier (30.73N, 79.32E) is a relatively large debris-covered glacier in the Garhwal region of

133 the central Himalaya (India). It has a total area of about 19 km^2, of which around 60% is debris covered.

134 The glacier spans a large elevation range of 3900 m to 6200 m, with the debris cover starting at elevation

135 of around 4500 to 4700 m depending on location. The debris layer is up to a meter or more in thickness,

136 and has an extent of about 11 km^2. This debris is mostly derived from weathering of large and steep

137 headwall and sidewalls of the glacier (Banerjee and Wani, 2018). Frequent avalanches and rockfalls efficiently

138 transport the debris onto the glacier. These avalanches, in fact, contribute to the majority of accumulation

139 in this glacier (Laha and others, 2017). The slope of the glacier in the debris-covered part is relatively

140 gentle. However, the clean-ice area above 4700m or so is very steep, and is inaccessible to us because of

141 the presence of ice-falls, and the danger of frequent avalanching. All of our ablation measurements are,

142 therefore, confined below 4700 m level.

143   Existing records suggest that the glacier is in a retreating phase since at least 1936, with an average frontal

144   retreat rate of about 6 m yr^{-1}(Nainwal and others, 2016). It has a relatively stagnant lower ablation zone,

145   with ice flow speeds of less than 5 m yr^{-1}. The lower ablation zone has been thinning at the rate of about

146   0.4 m per year over the past half a century or so (Nainwal and others, 2016).

147   All of the above characteristics are quite typical of debris-covered glaciers in the Himalaya (Scherler and

148   others, 2011a), and Satopanth Glacier can be considered a representative debris-covered Himalayan glacier.

4. FIELD DATA

149

150   Glaciological mass-balance measurement on Satopanth Glacier was initiated in the ablation season of 2014

151   with a small number of bamboo stakes, and is continuing until now with the network being extended to

152   up to about 60 stakes. Most of the stakes are arranged into 10 transverse lines at the main trunk below

153   4600m elevation, and a few lines across some of the tributaries. Each of these lines consists of about five

154   stakes. Most of the stakes are in the debris-covered parts, with measured debris thickness at stake locations

155   varying between 0.02 m to 1.14 m.

156   To install the stakes, we dug pits in the supraglacial debris exposing the glacial ice, drilled holes into

157   the ice using a Heucke steam drill, and inserted bamboo stakes. Each stake is approximately 2 m in length

158   and depending on location up to 3 stakes, joined by binding wire, were inserted into the drill hole. After

159   installation the pits were back-filled with debris. Subsequently, the height of the stakes above the debris

160   surface was monitored biweekly, with an accuracy of about 2 cm (Fig. B1). Due to the size of the glacier,

161   each set of measurements took about two to three days to complete depending on weather conditions. The

162   stake positions were monitored using a pair of Trimble R6 Global Navigation Satellite System receivers.

163   One specific problem encountered due to the local variability of debris thickness was that once a stake

164   was about to melt out, it was not possible to install a stake at a nearby location with the same debris

165   thickness and maintain continuity of the ablation data from that location. The nearby locations would

166   invariably have different debris thickness values, and thus, different ablation rates. Also, debris interfered

167   with stability of the stakes in various ways. For example, the bottom of the debris layer was typically

168   saturated with meltwater, and would cause some of the stakes to rot and break. This problem could be

169   mitigated by using painted stakes. Sometimes a stake would not fall off even when they have fully melted

170   out of the ice, remaining planted in the thick debris instead. However, such cases could be identified because

171   these stakes, once melted out of the ice, yielded a vanishingly low ablation rate. Overall, due to issues like

lost or broken stakes, delay in re-installing fallen stakes, bad weather conditions, equipment malfunctions etc. several data gaps have crept in our records.

In each ablation season, we began our periodic measurements during the last week of May and continue till the end of October. In the beginning of ablation period to measure the ablation of sub-debris ice, we kept to the snow-free stakes in the lower part of the glacier, and progressively moved up as upper stakes become snow free. Depending on year, by mid June to beginning of July, all the stakes become accessible.

The pits dug for installation of stakes and re-installation of fallen stakes were utilised to measure the debris thickness distribution. Until now, we have measured debris thickness at 191 locations. However, these pits are not uniformly distributed across the glacier ablation zone. They are mostly in the neighbourhood of the stakes along the transverse transects mentioned above (See Fig. 1).

5. DATA ANALYSIS

5.1. Characterisation of the spatial variability of debris-thickness

To estimate debris-thickness distribution, we binned the thickness data from the pits. The bin sizes varied from 5 cm for thin debris to 10, 15, and 25 cm as debris thickens (Fig. B2). This does not compromise the accuracy of mass-balance estimates as the variation of ablation rate with debris thickness is weaker for thicker debris (eq. 1). To analyse the variability of debris distribution at smaller spatial scales, we partitioned the entire debris-covered ablation zone into five subzones, such that for each of these subzones we have at least about 30 point-measurements of debris thickness available (Fig. 1), which were used to compute the frequency distribution of debris thickness at each of the subzones (Fig. B2). We acknowledge that the choice of the zone boundaries are somewhat arbitrary and that adds to the uncertainty in the mass balance computation. Accordingly, we considered a large (30%) uncertainty in the area of the subzones while estimating the errors in our computation of sub-debris ablation as described later.

5.2. Outliers in the ablation rate data

We have removed a few outliers in the stake data before further analysis. Some of the outliers are related to broken or melted-out stakes. Due to the thick debris layer, a few of the stakes remained standing after melting out and showed spuriously low or zero ablation rate. Some of the outliers were also due to likely mistakes while taking the reading manually. We tried to maintain photographic records of each measurement with scale, and a few mistakes could be corrected using such photographs. However, in some cases the quality of the field photographs were not good enough or photographs could not be taken, and we

Table 1. A summary of ablation data from the debris-covered part, and estimates of mean sub-debris ablation rate using method-I that uses elevation-dependent interpolation (b_I) and method-II that uses debris-thickness-dependent interpolation (b_{II}). See text for further details. Note that total observation period for each of the years are given in Julian day, and values of root mean square of fit residuals (RMSD) and adjusted R^2 are averaged over all the observations.

Year	Total obs. period	Num. of Obs.	Total stakes used	Total num. of records	Mean records per obs.	b_I (cm d^{-1})	RMSD (cm d^{-1})	Adj. R^2	b_{II} (cm d^{-1})	RMSD (cm d^{-1})	Adj. R^2
2015	148–282	8	55	262	32	1.25 ± 0.14	0.60	0.75	1.52 ± 0.20	0.41	0.88
2016	142–298	11	73	383	34	1.35 ± 0.17	0.77	0.76	1.70 ± 0.30	0.52	0.89
2017	145–297	10	83	334	33	1.56 ± 0.17	0.60	0.80	1.51 ± 0.20	0.45	0.89

201 preferred to discard the individual observations in case it showed unusually large deviations compared to
202 neighbouring stakes. Finally, we have 262, 383, and 334 ablation measurements available from the debris-
203 covered ablation zone during the ablation season of 2015, 2016, and 2017, respectively. The number of
204 ablation rate measurements from the debris-free part of the glacier is 24, 70, and 45, respectively.

205 **5.3. Relative performance of elevation and debris-thickness dependent**
206   **parameterisations of ablation rate**

207 The previous discussions on the influence of elevation and debris-thickness variability indicate that the best
208 method to obtain an accurate estimate of local sub-debris ablation rate anywhere in the debris-covered
209 ablation zone would be to parameterise ablation as a function of both elevation and debris thickness.
210 In practice, however, utility of such a method is limited as, for example, one needs the joint probability
211 distribution of both elevation and debris thickness to obtain glacier wide mean ablation. While, elevation
212 distribution may easily be obtained with remote-sensing methods, it is difficult to obtain the debris-
213 thickness distribution within each of the elevation bands. With field methods it is practically impossible to
214 get the distribution for each elevation band as that would require digging a very large number of pits. The
215 remote-sensing methods to determine debris thickness either do not work well in the thick debris ($\gtrsim 50cm$)
216 limit, or have significantly large uncertainty in this limit (Rounce and others, 2018). A way out of this

217   problem is possible in case either the variability of elevation or that of debris-thickness has a dominant

218   control over the local ablation rate variability - Then point-scale ablation data can be parameterised as

219   function of a single variable only, and the knowledge of the distribution of that specific variable is sufficient

220   to compute glacier-wide ablation.

221   To check whether it is the local elevation or the debris thickness that has stronger controls observed

222   ablation rate variation, we fitted all the ablation data for any given observation period separately to

223   an elevation-dependent and a debris-dependent function. Following standard glaciological protocol, the

224   elevation-dependent form $(b_z(z))$ was taken to be a quadratic polynomial in elevation (Kaser and others,

225   2003). The debris-dependent $(b_d(d))$ fit function was assumed to be of the form given in eq. (1) (Anderson

226   and Anderson, 2016). To quantify the goodness of the fits, we computed the root-mean-squared deviations

227   (RMSD) of the observed versus fitted ablation rates over all the data points. The adjusted R^2 for each of the

228   fits were also computed and compared between the methods. We also analysed the correlation coefficients

229   among debris thickness, elevation and ablation rate.

5.4. Computation of mean specific ablation over the debris-covered area with elevation-dependent interpolation (method-I)

232   We denote the standard glaciological mass-balance estimation protocol (Kaser and others, 2003) as method-

233   *I*. Here, for each of the measurement periods $(t_i - \Delta t_i, t_i)$, we collated all the available stake data from

234   the debris covered portion of the ablation zone, and fitted them to a smooth (three-parameter) quadratic

235   function of elevation $b_z(z, t_i)$ (eg, Fig. 3a). The mean specific ablation rate is obtained by averaging over

236   the hypsometry of the debris-covered part of the ablation zone and over all the measurement periods as

237   follows,

$$b_I = \left(\sum_j A_j \sum_i b_z(z_j, t_i)\Delta t_i \right) / \sum_i \sum_j A_j \Delta t_i, \tag{2}$$

238   where, A_j is the map area within the elevation band $(z_j,\ z_j + \Delta z)$.

239   To estimate the uncertainty in b_I due to the corresponding uncertainties in measurement of ablation at

240   the stakes and that in the area-elevation distribution, we employed a Monte Carlo method. We repeated

241   the steps outlined above 1000 times, but each time adding an independent zero-mean Gaussian noise to

242   the individual observations of ablation, and the area fraction at each bin. The Gaussian noise in ablation

243   data was assumed to have a standard deviation equal to twice the estimated measurement uncertainty

of each stake-height observation (estimated to be ~ 2 cm). Similarly, a nominal 20% uncertainty in area-elevation distribution were incorporated with the latter random noise. This uncertainty is partly due to the uncertainty in mapping the glacier boundary (particularly in the debris-covered parts), and due the uncertainty in Cartosat-1 digital elevation model (https://bhuvan.nrsc.gov.in). Another source of uncertainty in the estimated total ablation was the uncertainties in the smooth quadratic fit function b_z. For each elevation bin, the RMSDs of the observed values from the fitted curve were averaged over the measurements periods, and this mean RMSD was assumed to be the corresponding prediction errors for each of the elevation bins. Again, a zero-mean random Gaussian noise with standard deviation equalling the mean RMSD was added to the interpolated values in the Monte Carlo. Twice the standard deviation of the set of 1000 b_I-values obtained in the Monte Carlo procedure was taken to be the 2σ uncertainty estimates.
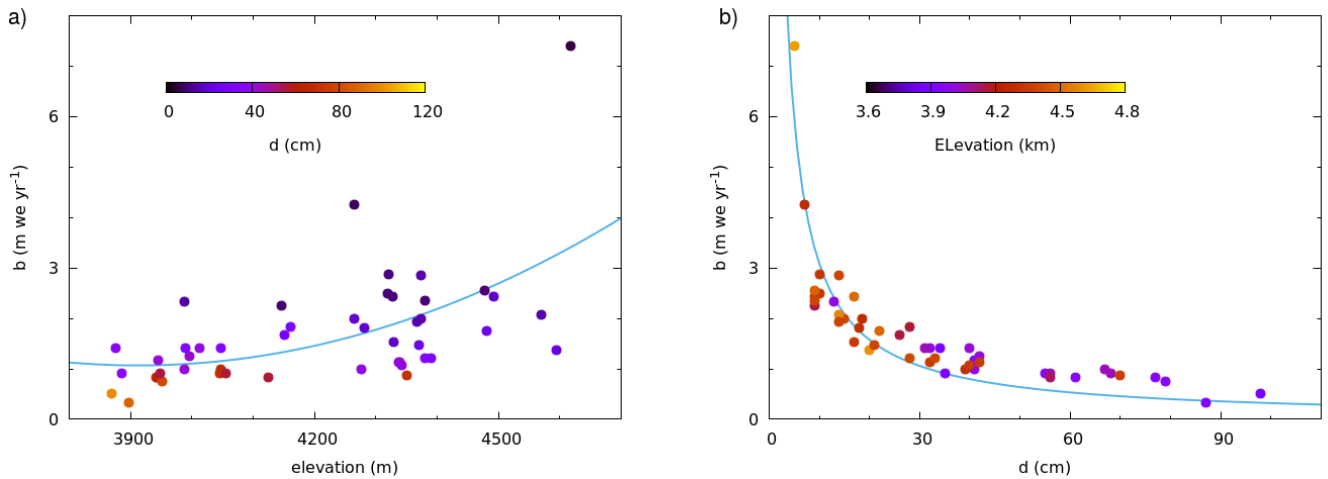
Fig. 3. Figure (a), and (b) show examples of smooth functions $b_I(z)$ and $b_{II}(d)$ fitted to the same ablation data set (Year 2016, Julian day 187±1). In sub-figure (a) symbol colors denote debris thickness, and in sub-figure (b) symbol colors represent elevation. See text for detailed discussion.

5.5. Computation of mean specific ablation over the debris-covered area with debris-thickness-dependent interpolation (method-II)

For the debris-covered part of the ablation zone, we used an alternative method where point-scale ablation-rate data were interpolated as a smooth function of debris thickness only. We denote this proposed method as method-II. In method-II, all the observed ablation rates in a given observation period were fitted to a smooth debris-thickness dependent function $b_d(d)$. We chose $b_d(d)$ to be of the form eq. 1 following Anderson and Anderson (2016). The parameters b_0 and d_0 were obtained separately for each observation

262 period (denoted by i). RMSD of the residuals, and R^2 were computed to quantify the goodness of fit. Then,

263 to obtain the mean sub-debris melt, the fitted b_d for each of the periods were averaged over the distribution

264 of area having debris-thickness value in a given range. To obtain the area distribution, we used the five

265 subzones (Fig. 1) and the frequency distribution of the debris thickness in each of these zones (Fig. B2).

266 The mean specific ablation rate over the debris-covered ablation zone was then computed as,

$$b_{II} = \left(\sum_{j,n} A_j^n \sum_i b_d(d_j, t_i) \Delta t_i \right) / \sum_{j,n} \sum_i A_j^n \Delta t_i, \tag{3}$$

267 where, A_j^n are the area with debris thickness values in the range $(d_j, d_j + \Delta d_j)$ for the n-th subzone (see

268 Fig. 1 for definition of the subzones).

269   The uncertainty in mean specific ablation estimates (b_{II}) due to measurement and mapping errors, and

270 prediction errors in the fitted forms were computed with 1000 Monte Carlo iterations with addition of

271 appropriate Gaussian noise as described above. The width of the noise in the ablation rate was again

272 assumed to be 4 cm. The prediction errors due to fitting were simulated in a similar manner using the

273 RMSD for each debris-thickness bin, that were averaged over all measurement periods. Since, demarcation

274 of the subzones is somewhat arbitrary, a larger 30% noise was added to the coefficients (A_j^n). Within each

275 subzone, the debris distribution was recomputed in each Monte Carlo step by adding a zero-mean Gaussian

276 noise with a standard deviation of 4 cm to the debris thickness value. Finally, the standard deviation of

277 the 1000 independent estimates as obtained in the Monte Carlo procedure was used to estimate the 2σ

278 uncertainty in b_{II}.

279 **5.6. Biases due to number of stakes used**

280 We have investigated the robustness of estimated b_I and b_{II} with respect to the number of stakes used

281 by a Monte Carlo method with repeated computation of the two quantities with randomly chosen subsets

282 of all the available stakes. First, we computed the net ablation rate over the debris-covered parts of the

283 ablation zone with all the available stakes (N) using both the methods (I and II) following the procedure

284 described above. Then, the net ablation computation for both the methods were repeated 300 times for

285 randomly chosen subsets of $3N/4$, $N/2$ and $N/4$ stakes. In case, the randomly chosen subset of stakes

286 did not have a single observation in any of the measurement intervals, that subset was ignored. The

287 distributions of the estimates for b_I and b_{II} for each of the sample sizes were then analysed to investigate

the possible uncertainties and biases in the result obtained as a function the number of stakes used for both the methods.

5.7. Calculation of net specific mass balance for the whole glacier

As discussed before, Satopanth is not an ideal glacier for mass-balance studies (Kaser and others, 2003) at least on three counts: 1) The presence of extensive supraglacial debris, 2) very strong avalanche contribution to mass balance, and 3) inaccessibility of the upper ablation zone and accumulation zone. These problems are quite typical in the Himalayan debris-covered glaciers (Laha and others, 2017), often making it difficult to estimate the corresponding net balance accurately (Azam and others, 2018). For Satopanth Glacier, the long-term mean of avalanche contribution to mass balance has been estimated (Laha and others, 2017). However, its inter-annual variation, which is likely to be significant, are not known. In addition, our data from the clean-ice areas were from a small number $(5-9)$ of stakes that spanned a limited elevation range of only about 150 m due to the inaccessibility of the upper reaches. These factors impeded an accurate estimation of net annual balance of the glacier. Nevertheless, we have obtained rough estimates of the net specific balance of the glacier using available data by extrapolation. We acknowledge that large extrapolation errors in the reported values are quite likely, and such extrapolation errors are difficult to estimate as well. The following procedure was used to obtain the approximate net specific balance. A smooth fit to the limited clean-ice ablation data as a function of both elevation and time was constructed. To do that, all the data from a given year were fitted separately to a linear z-dependent mass-balance profile $(b_1(z))$, and a fourth-order polynomial in time $(b_2(t))$. For the elevation-dependent fit the stake-level data were binned with a binsize of 25 m before fitting. Subsequently, these two fitted functions were utilised to construct the following smooth interpolating function,

$$b_c(z,t) = b_2(t) + b_1(z) - b_1(z_0). \tag{4}$$

Here, z_0 was tuned to minimise the total squared misfit with respect to all the observed clean-ice ablation rate in a ablation season. The RMSD of the fits were computed to obtain a measure of uncertainty of the fits. The values predicted by the best-fit smooth form (eq. 4) were plotted against the corresponding observed ones to visually inspect the fit quality as well. Finally, the fitted function (eq. 4) was averaged over the total melt season, using the area-elevation distribution of the clean-ice region. We extrapolated the clean-ice melt data, with a cut-off of 150 cm/yr in net accumulation (Laha and others, 2017). The net specific

315 balance for the whole glacier was obtained by averaging the melt estimates for debris-covered and debris-

316 free parts, weighted by the corresponding area fractions. The available estimate of the long-term avalanche

317 contribution to accumulation (Laha and others, 2017) was added to the result to obtain the reported

318 estimates of net specific balance of Satopanth glacier. We re-emphasise that due to the the possible large

319 extrapolation errors the net specific ablation estimates are rather uncertain, and the obtained values are

320 only rough estimates. However, we checked the consistency of these estimates with available decadal-scale

321 geodetic mass balance(Brun and others, 2017). We also compare the estimates of mass-balance gradient

322 and ELA, and their interrelationship to those of neighbouring glaciers where such data is available.

6. RESULTS AND DISCUSSIONS

6.1. Spatial variability of debris-thickness

325 The measured debris thickness values in the pits ranged from a couple of cm to more than 100 cm, with a

326 highest observed debris thickness of 114 cm. In general, the debris layer thickened downglacier (Fig. 2b).

327 The mean debris thickness of the five subzones defined in Fig. 1 increased with decreasing mean elevation,

328 varying from 7 cm to 61 cm. This trend of a general downglacier increase in debris thickness is also evident

329 from the fact the debris thickness and elevation at all the 191 pits were anti-correlated with a correlation

330 coefficient of -0.64 ($p < 0.0001$).

331 The above increase of the local mean of debris thickness downglacier is accompanied by a comparable

332 increase in the local variability of debris thickness. The standard deviation of debris thickness within each of

333 the subzones increased along with with the corresponding mean, such that it was at least half the mean or

334 more (Fig. 2b). To give an example, in the lowermost subzone, the observed debris-thickness varied between

335 2 cm and 114 cm, with a mean of 61 cm and a standard deviation of 30 cm. The observed debris-thickness

336 distribution in each of the subzones are given in the supplementary Fig. B2.

337 This trend of nearly monotonic downglacier increase of both the mean debris thickness and its local

338 spatial variability, is consistent with data from other debris-covered glaciers in the Himalaya and elsewhere

339 (Mihalcea and others, 2006; Zhang and others, 2011; Nicholson and Mertes, 2017; Banerjee and Wani, 2018;

340 Nicholson and others, 2018). The increasing trend of the local mean debris thickness has been explained in

341 terms of the emergence of englacial debris, and the decline of glacier ice-flow velocity towards the terminus

342 (Kirkbride and Deline, 2013; Anderson and Anderson, 2016, 2018). However, a theoretical understanding

343 or model reproduction of the fluctuating part of the debris-thickness distribution discussed above is not

Table 2. A summary of ablation data from the clean-ice parts of Satopanth Glacier and estimates of mean ablation rate over the clean ice area. The estimated net specific balance of the glacier are also listed. Note that total observation period for each of the years are given in Julian day. See text for further details and clarifications.

Year	Total obs. period	Total stakes used	Total num. of records	Ablation gradient (m yr^{-1} per 100 m)	ELA (m)	Clean-ice ablation (cm d^{-1})	Net balance (m w.e. yr^{-1})
2015	186–260	5	24	0.8	5200	2.3 ± 0.2	-0.2 ± 0.6
2016	159–277	9	70	0.6	5480	2.4 ± 0.2	-0.8 ± 0.6
2017	167–296	8	45	0.6	5430	2.6 ± 0.2	-0.6 ± 0.6

available at present. A critical role of gravity-driven non-diffusive debris redistribution processes, induced by the dynamic thermokarst topography that characterises the debris-covered ablation zone, is expected in creating and maintaining the observed inhomogeneous debris distribution (Moore, 2018; Nicholson and others, 2018). A detailed characterisation of the fluctuating part of the debris distribution would be presented in a subsequent paper.

6.2. Dependence of mass balance on elevation vis-a-vis debris thickness

Our analysis showed that the debris-thickness dependent smooth function $b_b(d)$ provided a better description of the mass balance variation than the elevation-dependent function $b_z(z)$ (Fig. 3 and supplementary Figs. B2 to B7) for all the observation periods, in the sense that the former obtains systematically higher R^2 for the fits. The ablation rate for any given period showed a larger scatter around the elevation-dependent fitted forms than the debris-thickness dependent forms. All the fitted profiles for all the three years are given in Supplementary Figs. B2 to B7 conform to this general trend. With debris-thickness dependent fits, the mean RMSD over all the fits in a year varied between 0.41 to 0.52 cm d^{-1} among the three years. In comparison, the corresponding RMSDs with elevation-dependent fits were about 50% higher, with mean values ranging between 0.60 to 0.77 cm d^{-1} for the years 2015, 2016, and 2017. The debris-thickness dependent fits obtained systematically smaller adjusted-R^2 as well (Table 1). These trends indicate that the variation of ablation rate over the debris-covered parts of Satopanth Glacier is better described by the debris-dependent form b_d than the elevation dependent form b_z.
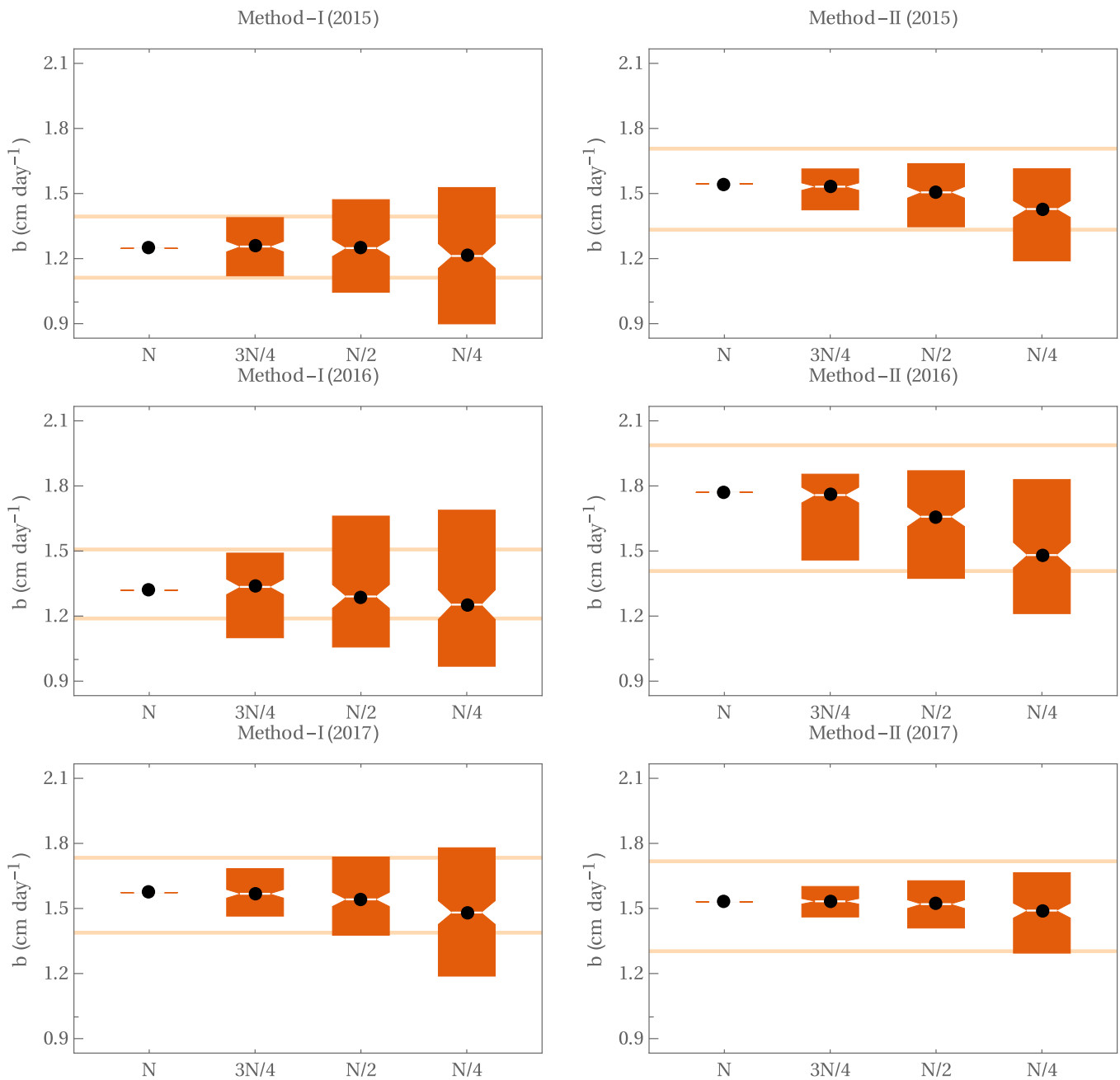
Fig. 4. The distribution of estimated sub-debris specific ablation over the ablation zone of Satopanth Glacier as computed using method-I and method-II for the three years. Horizontal axis denotes the number of stakes used in the calculations. Either all the N stakes, or 300 random subsets with $3N/4$, $N/2$ and $N/4$ stakes each were used to compute the mean sub-debris ablation rate. Values of N were 55, 73, and 83 for 2015, 2016 and 2017, respectively. The vertical bars depict the spread of the distribution from 5 to 95 percentile. The black dots represent the median value. Horizontal orange lines show the 2σ confidence band for the estimated ablation rate (see Table 1) for reference.

362   In addition, the correlation between variation of debris-thickness and that of ablation rate was
363   systematically stronger (-0.53 to -0.57; $p < 0.0001$) than that between the variations of elevation and

364 ablation rates (0.32 to 0.44,$p < 0.0001$) for all the three years. This strengthens the above claim that local

365 debris thickness is a better predictor of local ablation rate.

366 The improved accuracy obtained with the debris-thickness dependent fitting functions in smooth-

367 ing/interpolating the sub-debris ablation data makes a strong case for using method-II which interpolates

368 ablation rate as a function of debris thickness alone for each of the observation periods to compute mean

369 sub-debris ablation. In fact, in this method the weaker elevation dependence of ablation rate is implicitly

370 taken in to account to some extent due to the anti-correlated variation of elevation and debris-thickness

371 observed (a correlation coefficient of $-0.64, p < 0.0001$).

372 Since, the overall properties of the debris-thickness distribution of Satopanth Glacier is similar to that of

373 other debris-covered Himalayan glaciers as discussed in the previous subsection, it may be expected that

374 the debris-thickness dependent interpolation would in general be a more accurate method on debris-covered

375 ablation zone of other glaciers as well. As mentioned before, an interpolation method that uses the joint

376 distribution of elevation and debris may be more accurate. However, from a practical point of view, it

377 may be difficult to obtain accurate debris-thickness distribution for each of the elevation bands through

378 field measurements due to logistical issues. Remote-sensing methods can be useful, but they are not very

379 accurate in the thick-debris limit (Rounce and others, 2018). In this context, method-II presented here may

380 be a good compromise.

381 ### 6.3. Mean sub-debris ablation using method-I and method-II

382 Method-I, which the standard glaciological method where ablation rates were interpolated as a function

383 of elevation (eq. 2), yielded mean ablation rate of 1.25 ± 0.14, 1.35 ± 0.17, and 1.56 ± 0.17cm d^{-1} for the

384 ablation season of 2015, 2016 and 2017, respectively, over the debris-covered part of the ablation zone.

385 While with method-II, which is based on a debris-thickness dependent interpolation (eq. 3), the estimated

386 mean sub-debris ablation for these three years were 1.52 ± 0.20, 1.70 ± 0.30, and 1.51 ± 0.20 cm d^{-1}. The

387 distribution of the values of generated in the Monte Carlo for the two methods are shown in supplementary

388 Fig. B9.

389 Despite the tighter fits obtained with the debris-dependent interpolation scheme used in method-II, the

390 differences between the estimates obtained in the two methods are not significant when the uncertainties in

391 the corresponding values are considered (Table 1). For the ablation seasons of 2015 and 2016, the estimated

392 values of b_I are about 20–25% smaller than corresponding estimates of b_{II}, while for 2017, b_I is a few percent

393 higher than b_{II}. However, none of these differences are significant given the uncertainties present in the

estiamates. This implies that the empirical elevation-dependent quadratic smooth interpolating function does well in predicting the mean ablation in any elevation band, even as it does not capture the variabilty of ablation rate within that elevation band. This could be because of the relatively large number of stakes used in this study, so that within each elevation band a few stakes with different debris thickness are available (Fig. B3-B5). The arrangement of stakes along transverse lines (Fig. 1) also helps in sampling the debris distribution within a elevation band better. If these arguments are correct, then discernible differences between estimates from the two methods may be present when data from only a few stakes are available. This is discussed in the next subsection.

We also note that despite the better fits to ablation data obtained in method-II, the relative uncertainties are somewhat higher in this method (13-18%) as compared to that in method-I (11-13%). This is likely related to possible large uncertainties in partitioning the debris-covered area into the subzones, and the limited number of debris-thickness measurements ($\sim$30) that are available for each of the subzones. The uncertainties of the method-II estimates would be brought down further with more detailed measurement of the debris-thickness distribution over the ablation zone.

6.4. Accuracy of the estimates as a function of the number of stakes

The total number of stakes where some ablation data were available (N) varied from 55 to 83 (Table 1). We note that this includes reinstalled stakes and the number of stakes available for any observation period was relatively smaller. The mean number of stakes in different observation periods was $\sim$ 30 (Table 1). In the numerical experiments, where only a fraction of available stakes were used for the ablation rate calculations, the estimated ablation for any given random subset of the data had biases for both the methods. Both positive and negative biases were observed depending on the chosen random subset, and the biases were systematically larger as the number of stakes used went down from N to $N/4$. For method-I, using $3N/4$ stakes the estimates were within the uncertainty band of ablation estimated with the full data set (Fig. 4) for 2015 and 2017. Only in 2016 some of the random subsets underestimate the mean ablation significantly. The observed deviations in this method were always significant for $N/2$ stakes. For method-II, the spread in the estimates from random subsets of the stakes were in general smaller compared to that in method-I. Here, even the subsets with $N/2$ stakes produced estimates that are within the uncertainty band (except in 2016). Only with $N/4$ stakes significant underestimation of mean ablation was observed for method-II. Generally larger uncertainties in 2016 may be related to the two observation periods where data from only about 10 stakes are available (Figs. B3 and B6).

As discussed in the previous subsection, debris-dependent fits work significantly better than the corresponding elevation-dependent forms. However, that did not translate to any significant differences between the net balance estimates from the two methods. In this context, the set of estimates using smaller subsets of the whole data as described above establishes a clear advantage of method-II over method-I. The method-II estimates are seen to be much more robust to a reduction in the number of stakes used. This is a consequence of the tighter fits obtained with the debris-dependent parameterisation. In contrast, the elevation-dependent smoothing procedure is able to capture the mean ablation in any given elevation band accurately only when a relatively large number of data points are available. With a small number of stakes the fluctuation caused by the variability of debris thickness does not get averaged out, resulting in possibly large bias in the mean ablation estimated using method-I as compared to that from method-II.

Based on our analysis, an optimal strategy to measure ablation over debris-covered ablation zone with an area of ~ 10 km^2, is to use about 20 to 30 stakes (i.e., 2-3 stakes per km^2). The key to an accurate ablation estimate is covering a range of debris thickness values and a careful mapping of the debris-thickness distribution. Note that with a smaller sized debris-covered glacier, the total number of stakes cannot be reduced proportionately, as sampling the range of debris-thickness values would become an issue. Another important point is to maintain the continuity of measurements - An observation period with a large number of missing stakes can be detrimental to the accuracy of the estimate.

6.5. Net balance for the whole glacier

The approximate net specific balance of Satopanth Glacier for each of the balance years was obtained by combining observed ablation in the debris-covered part, extrapolated specific balance over the clean-ice area, and the long-term avalanche strength estimate for the glacier (1.8 ± 0.5 m w.e./yr (Laha and others, 2017)). The estimated net specific balance values were -0.2 ± 0.6, -0.8 ± 0.6, and -0.6 ± 0.6 m w.e. yr^{-1} for the year 2015, 2016, and 2017, respectively. Here, we have assumed ice density of 900 kg m^{-1}. It is notable that the mean specific ablation rate over the clean-ice area ($2.3 - 2.4$ cm d^{-1}; see Table 2) is significantly larger than the corresponding sub-debris specific ablation ($1.5 - 1.7$ cm d^{-1}; see Table 1), despite the relatively lower elevation of the debris-covered area. This is consistent with the strong insulating effects of the supraglacial debris layer discussed at the outset.

It was observed that the smoothing/fitting procedure adopted for the clean-ice region provided a reasonable description of the variability of ablation rate as a function of both time and elevation (Fig. B10 -B.12), with RMSD varying between 0.5 to 0.8 cm d^{-1}. In addition, the estimated net mass balance values

454 compared well with other independent measurements. For example, the mean mass balance of -0.5 ± 0.6 m

455 w.e. yr^{-1} over the three years was comparable to the geodetic thinning rate of 0.52 m yr^{-1} for Satopanth

456 Glacier over the period of 2000 to 2016 as computed using data from Brun and others (2017). It was also

457 consistent with reported thinning rate of 0.4 m yr^{-1} over the lower ablation zone of the glacier between

458 1962 to 2013.

459   The estimated equilibrium line altitude (ELA) at Satopanth Glacier during the observation period varied

460 between 5200 m to 5480 m (Table 2) with a mean value of 5370 m. The mean ELA at Satopanth Glacier

461 is somewhat higher than the observed mean ELA in the four other central Himalayan glaciers that are

462 within about 50km radius. For example, mean ELA of 5066, 5068, 4588 and 4845 m have been reported for

463 Dokriani, Chorabari, Tipra, and Dunagiri Glaciers (Pratap and others, 2016). This could be indicative of

464 possible large differences in local precipitation due to the complex topography. Relatively high mean ELA

465 in the range of 5534 m to 5625 m were also reported in Mera, Pokalde, and West Changri Nup Glaciers

466 in Khumbu region. A relatively large inter-annual variability of ELA ($\sim$ 150 m) is a feature common to

467 both Satopanth and Mera Glaciers (Sherpa and others, 2017), though only three data points are available

468 for Satopanth Glacier. In contrast, the reported inter-annual variability of ELA at the four glaciers nearby

469 Satopanth Glacier were relatively low, e.g. only 9 m on Chorabari Glacier (Pratap and others, 2016).

470   The annual estimates of net balance and ELA for Satopanth glacier showed a strongly linear relationship

471 (supplementary Fig. A13). This may be interpreted as a sign of the reliability of net balance estimate

472 (Azam and others, 2018). Among the glaciers mentioned above only Dokriani, Mera and Pokalde Glacier

473 show similar anticorrelations between ELA and net balance. An extrapolation of observed the linear trend

474 showed that a ELA value of about 5050 m would correspond to zero net balance of Satopanth Glacier.

475   The estimated net specific balance of Satopanth glacier during 2015 matched with the preliminary

476 estimate reported by Laha and others (2017). The previous estimate was obtained with data from only 40

477 stakes that had continuous record over the whole ablation season. In particular, clean ice melt was available

478 only from two stakes. Two linear profiles were fitted separately to clean-ice and sub-debris melt data and

479 these were averaged over the clean and debris-covered area, respectively, to compute to total melt. We

480 consider the present method of net balance estimation more accurate, although the value remains the same

481 as reported earlier (Laha and others, 2017).

7. CONCLUSIONS

We measured surface ablation on debris-covered Satopanth Glacier (central Himalaya) using a network of up to 56 stakes during the ablation season of 2015, 2016, and 2017. The debris-thickness distribution was also obtained by direct field measurements on 191 locations. Using the extensive ablation data, we established that a debris-thickness dependent smoothing curve performs significantly better than a elevation-dependent regression, in describing the spatial variability of surface ablation at any given observation period. We utilised the debris-dependent smooth fits to the ablation data, averaged over the debris-thickness distribution over the glacier surface, to obtain mean sub-debris ablation rate on Satopanth Glacier of 1.52 ± 0.20, 1.70 ± 0.30, and 1.51 ± 0.20 cm d^{-1} during 2015, 2016, and 2017. In comparison, the standard glaciological method obtained ablation rate of 1.25 ± 0.14, 1.35 ± 0.17, and 1.56 ± 0.17cm d^{-1} for the three years. While the differences in estimates from the two methods were not significant within the uncertainties, biases were not negligible if the number of stakes with data are low. A density of 2 to 3 stakes per km^2 or more, such that data from a total of about 20-30 stakes are available, are sufficient for an accurate estimate. However, the debris-thickness at the stakes must span a wide range. The accuracy of the estimates using debris-dependent method may be improved with detailed measurement of the debris thickness distribution. We estimated approximate net specific balance of Satopanth glacier for the years 2015, 2016, and 2017 to be -0.2 ± 0.6, -0.8 ± 0.6, and -0.6 ± 0.6 m w.e. yr^{-1}.

8. ACKNOWLEDGEMENTS

All the ablation data presented in the paper would be made public after publication of the paper.

REFERENCES

Anderson, R. S., and Anderson, L. S. (2016). Modeling debris-covered glaciers: response to steady debris deposition. The Cryosphere, 10(3), 1105.

Anderson, L. S., and Anderson, R. S. (2018). Debris thickness patterns on debris-covered glaciers. Geomorphology, 311, 1-12.

510 Azam, M. F., Wagnon, P., Berthier, E., Vincent, C., Fujita, K., and Kargel, J. S. (2018). Review of the status and

511　　mass changes of Himalayan-Karakoram glaciers. Journal of Glaciology, 64(243), 61-74.

512 Banerjee, A., and Shankar, R. (2013). On the response of Himalayan glaciers to climate change. Journal of Glaciology,

513　　59(215), 480-490.

514 Banerjee, A. (2017). Brief communication: Thinning of debris-covered and debris-free glaciers in a warming climate.

515　　The Cryosphere, 11(1), 133-138.

516 Banerjee, A., and Wani, B. A. (2018). Exponentially decreasing erosion rates protect the high-elevation crests of the

517　　Himalaya. Earth and Planetary Science Letters, 497, 22-28.

518 Benn, D. I. and others(2012). Response of debris-covered glaciers in the Mount Everest region to recent warming,

519　　and implications for outburst flood hazards. Earth-Science Reviews, 114(1), 156-174.

520 Benn, D. I., Kirkbride, M. P., Owen, L. A., and Brazier, V. (2003). Glaciated valley landsystems. Glacial landsystems,

521　　372-406.

522 Benn, D. I., and Lehmkuhl, F. (2000). Mass balance and equilibrium-line altitudes of glaciers in high-mountain

523　　environments. Quaternary International, 65, 15-29.

524 Brock, B. W., Mihalcea, C., Kirkbride, M. P., Diolaiuti, G., Cutler, M. E., and Smiraglia, C. (2010). Meteorology and

525　　surface energy fluxes in the 2005-2007 ablation seasons at the Miage debris-covered glacier, Mont Blanc Massif,

526　　Italian Alps. Journal of Geophysical Research: Atmospheres, 115(D9).

527 Brun, F., Berthier, E., Wagnon, P., Kääb, A., and Treichler, D. (2017). A spatially resolved estimate of High Mountain

528　　Asia glacier mass balances from 2000 to 2016. Nature geoscience, 10(9), 668-673.

529 Cogley, J.C., 1999: Effective sample size for glacier mass balance. Geografiska Annaler, 81A: 497-507.

530 Collier, E., Nicholson, L. I., Brock, B. W., Maussion, F., Essery, R., and Bush, A. B. G. (2014). Representing moisture

531　　fluxes and phase changes in glacier debris cover using a reservoir approach. The Cryosphere, 8(4), 1429-1444.

532 Dobhal, D. P., Mehta, M., and Srivastava, D. (2013). Influence of debris cover on terminus retreat and mass changes

533　　of Chorabari Glacier, Garhwal region, central Himalaya, India. Journal of Glaciology, 59(217), 961-971.

534 Evatt, G. W., Abrahams, D., Heil, M., Mayer, C., Kingslake, J., Mitchell, S. L., ... and Clark, C. D. (2015). Glacial

535　　melt under a porous debris layer. Journal of Glaciology, 61(229), 825-836.

536 Fountain, A. G., and Vecchia, A. (1999). How many stakes are required to measure the mass balance of a glacier?.

537　　Geografiska Annaler: Series A, Physical Geography, 81(4), 563-573.

538 Fujita, K., and Sakai, A. (2014). Modelling runoff from a Himalayan debris-covered glacier. Hydrology and Earth

539　　System Sciences, 18(7), 2679.

540 Fyffe, C. L., Reid, T. D., Brock, B. W., Kirkbride, M. P., Diolaiuti, G., Smiraglia, C., and Diotri, F. (2014). A

541　　distributed energy-balance melt model of an alpine debris-covered glacier. Journal of Glaciology, 60(221), 587-602.

542 Gardelle, J., Berthier, E., Arnaud, Y., and Kaab, A. (2013). Region-wide glacier mass balances over the Pamir-
543   Karakoram-Himalaya during 1999-2011. The Cryosphere, 7(6), 1885-1886.

544 Juen, M., Mayer, C., Lambrecht, A., Han, H., and Liu, S. (2014). Impact of varying debris cover thickness on ablation:
545   a case study for Koxkar Glacier in the Tien Shan. The Cryosphere, 8(2), 377.

546 King, O., Dehecq, A., Quincey, D., and Carrivick, J. (2018). Contrasting geometric and dynamic evolution of lake
547   and land-terminating glaciers in the central Himalaya. Global and Planetary Change.

548 Kirkbride, M. P., and Deline, P. (2013). The formation of supraglacial debris covers by primary dispersal from
549   transverse englacial debris bands. Earth Surface Processes and Landforms, 38(15), 1779-1792.

550 Kraaijenbrink, P. D. A., Bierkens, M. F. P., Lutz, A. F., and Immerzeel, W. W. (2017). Impact of a global temperature
551   rise of 1.5 degrees Celsius on Asia's glaciers. Nature, 549(7671), 257.

552 Haidong, H., Yongjing, D., and Shiyin, L. (2006). A simple model to estimate ice ablation under a thick debris layer.
553   Journal of Glaciology, 52(179), 528-536.

554 Heimsath, A. M., and McGlynn, R. (2008). Quantifying periglacial erosion in the Nepal high Himalaya.
555   Geomorphology, 97(1-2), 5-23.

556 Immerzeel, W. W., Van Beek, L. P. H., Konz, M., Shrestha, A. B., and Bierkens, M. F. P. (2012). Hydrological
557   response to climate change in a glacierized catchment in the Himalayas. Climatic change, 110(3-4), 721-736.

558 Kaser, G., Fountain, A., and Jansson, P. (2003). A manual for monitoring the mass balance of mountain glaciers (p.
559   137). Paris: Unesco.

560 Laha, S. and others(2017). Evaluating the contribution of avalanching to the mass balance of Himalayan glaciers.
561   Annals of Glaciology, 58(75pt2), 110-118.

562 Lejeune, Y., Bertrand, J. M., Wagnon, P., and Morin, S. (2013). A physically based model of the year-round surface
563   energy and mass balance of debris-covered glaciers. Journal of Glaciology, 59(214), 327-344.

564 Mattson, L. E., Gardner, J. S., and Young, G. J. (1993). Ablation on debris covered glaciers: an example from
565   the Rakhiot Glacier, Punjab, Himalaya. IAHS Publ. 218 (Symposium at Kathmandu 1992 - Snow and Glacier
566   Hydrology), 289-296.

567 Mihalcea, C., Mayer, C., Diolaiuti, G., Lambrecht, A., Smiraglia, C., and Tartari, G. (2006). Ice ablation and
568   meteorological conditions on the debris-covered area of Baltoro glacier, Karakoram, Pakistan. Annals of Glaciology,
569   43, 292-300.

570 Miles, E. S., Willis, I. C., Arnold, N. S., Steiner, J., and Pelliccciotti, F. (2017). Spatial, seasonal and interannual
571   variability of supraglacial ponds in the Langtang Valley of Nepal, 1999–2013. Journal of Glaciology, 63(237),
572   88-105.

573 Moore, P. L. (2018). Stability of supraglacial debris. Earth Surface Processes and Landforms, 43(1), 285-297.

574 Naito, N., Nakawo, M., Kadota, T., and Raymond, C. F. (2000, September). Numerical simulation of recent shrinkage
575   of Khumbu Glacier, Nepal Himalayas. In Debris-covered Glaciers: Proceedings of an International Workshop Held
576   at the University of Washington in Seattle, Washington, USA, 13-15 September 2000 (No. 264, p. 245). IAHS.

577 Nainwal, H. C., Banerjee, A., Shankar, R., Semwal, P., and Sharma, T. (2016). Shrinkage of Satopanth and Bhagirath
578   Kharak glaciers, India, from 1936 to 2013. Annals of Glaciology, 57(71), 131-139.

579 Nakawo, M., and Young, G. J. (1982). Estimate of glacier ablation under a debris layer from surface temperature
580   and meteorological variables. Journal of Glaciology, 28(98), 29-34.

581 Nicholson, L., and Benn, D. I. (2013). Properties of natural supraglacial debris in relation to modelling sub-debris
582   ice ablation. Earth Surface Processes and Landforms, 38(5), 490-501.

583 Nicholson, L., and Mertes, J. (2017). Thickness estimation of supraglacial debris above ice cliff exposures using a
584   high-resolution digital surface model derived from terrestrial photography. Journal of Glaciology, 63(242), 989-998.

585 Nicholson, L. I., McCarthy, M., Pritchard, H., and Willis, I.: Supraglacial debris thickness variability: Impact on
586   ablation and relation to terrain properties, The Cryosphere Discuss., https://doi.org/10.5194/tc-2018-83, in review,
587   2018.

588 Nuimura, T., Fujita, K., Yamaguchi, S., and Sharma, R. R. (2012). Elevation changes of glaciers revealed by
589   multitemporal digital elevation models calibrated by GPS survey in the Khumbu region, Nepal Himalaya, 1992-
590   2008. Journal of Glaciology, 58(210), 648-656.

591 Oerlemans, J. (2001). Glaciers and climate change. CRC Press.

592 Østrem, G. (1959). Ice melting under a thin layer of moraine, and the existence of ice cores in moraine ridges.
593   Geografiska Annaler, 41(4), 228-230

594 Pratap, B., Dobhal, D. P., Bhambri, R., Mehta, M., and Tewari, V. C. (2016). Four decades of glacier mass balance
595   observations in the Indian Himalaya. Regional Environmental Change, 16(3), 643-658.

596 Reid, T. D., and Brock, B. W. (2014). Assessing ice-cliff backwasting and its contribution to total ablation of debris-
597   covered Miage glacier, Mont Blanc massif, Italy. Journal of Glaciology, 60(219), 3-13.

598 Reynolds, J. M. (2000). On the formation of supraglacial lakes on debris-covered glaciers. IAHS publication, 153-164.

599 Rounce, D. R., King, O., McCarthy, M., Shean, D. E., and Salerno, F. (2018). Quantifying Debris Thickness of
600   Debris-Covered Glaciers in the Everest Region of Nepal Through Inversion of a Subdebris Melt Model. Journal of
601   Geophysical Research: Earth Surface.

602 Rowan, A. V. and others(2018). Multiannual observations and modelling of seasonal thermal profiles through
603   supraglacial debris in the Central Himalaya. The Cryosphere Discussion. In review.

604 Sakai, A., Takeuchi, N., Fujita, K., and Nakawo, M. (2000). Role of supraglacial ponds in the ablation process of a
605   debris-covered glacier in the Nepal Himalayas. IAHS PUBLICATION, 119-132.

606 Scherler, D., Bookhagen, B., and Strecker, M. R. (2011). Spatially variable response of Himalayan glaciers to climate

607   change affected by debris cover. Nature geoscience, 4(3), 156-159.

608 Scherler, D., Bookhagen, B., and Strecker, M. R. (2011). Hillslope-glacier coupling: The interplay of topography and

609   glacial dynamics in High Asia. Journal of Geophysical Research: Earth Surface, 116(F2).

610 Sherpa, S. F. and others(2017). Contrasted surface mass balances of debris-free glaciers observed between the southern

611   and the inner parts of the Everest region (2007–15). Journal of Glaciology, 63(240), 637-651.

612 Zhang, Y., Fujita, K., Liu, S., Liu, Q., and Nuimura, T. (2011). Distribution of debris thickness and its effect on ice

613   melt at Hailuogou glacier, southeastern Tibetan Plateau, using in situ surveys and ASTER imagery. Journal of

614   Glaciology, 57(206), 1147-1157.

615 # APPENDIX A. DETAILS OF THE UNCERTAINTY ANALYSIS

616 ## A.1. Method I

617 We divide the observed region into N_e elevation bands. The bands are 100 m wide and the area of each

618 band, A_j^z is shown in Fig. 2a.

619   The observation times are denoted by t_i, $i = 1, \ldots, N_t$ and the time periods between them by

620 $\Delta t_i \equiv t_{i+1} - t_i$. The observation times are given in Figs. (B2-B7)

    Equation (2) in the main text gives the expression for the average ablation rate estimated using method

I. It can be written as,

$$b_I = \frac{1}{A} \sum_{j=1}^{N_e} A_j^z \, \bar{b}_z(z_j) \tag{A1}$$

$$\bar{b}_z(z_j) = \frac{1}{T} \sum_{i=1}^{N_t} b_z(z_j, t_i) \Delta t_i \tag{A2}$$

621 where A is the total area of the observation region, $A = \sum_{j=1}^{N_e} A_j$ and T is the total observation time

622 period, $T = \sum_i \Delta t_i$.

623   The uncertainty in b_I is computed using the the following algorithm:

624   For $n = 1 - 1000$

625 1. Compute the parameters, a_{ni}, b_{ni}, c_{ni} by fitting the data, $b^{obs}(z_m, t_i) + \Delta b^{obs}(z_m, t_i)$ to the quadratic

626   function $b_{zn}(z, t_i) = a_{ni} + b_{ni}z + c_{ni}z^2$. Where $b^{obs}(z_m, t_i)$ is the observed ablation at the mth stake at

627   elevation z_m, during the ith time period and $\Delta b^{obs}(z_m, t_i)$ is a Gaussian noise with standard deviation

628   4 cm.

2. Compute the RMSD at each time period,

$$\Delta b_{zn}(t_i) = \sqrt{\frac{1}{N_e} \sum_m \left(b_{zn}(z_m, t_i) - b^{obs}(z_m, t_i) \right)^2} \tag{A3}$$

3. Compute the average RMSD over all the time periods,

$$\Delta \bar{b}_{zn} = \sqrt{\frac{1}{N_e} \sum_i \left(\Delta b_{zn}(t_i) \right)^2} \tag{A4}$$

4. Compute the net average ablation rate, b_{In},

$$b_{In} = \frac{\left(\sum_j A_j + \Delta A_{jn} \right) \left(\bar{b}_n(z_j) + \Delta \bar{b}_n(z_j) \right)}{\sum_j \left(A_j + \Delta A_{jn} \right)} \tag{A5}$$

where A_j is the estimated area of the jth elevation zone, ΔA_{jn} is a Gaussian noise with standard deviation equal to $0.2 A_j$ and $\Delta \bar{b}_n(z_j)$ is a Gaussian noise with standard deviation equal to $\Delta \bar{b}_{zn}$

5. The mean value and standard deviation of this distributions of 1000 values of b_I are the reported mean values of the most probable value of b_I and its uncertainty. The distributions are plotted in Fig. B9.

A.2. Method II

1. We divide the observation region into 5 zones, shown in Fig. 1. The debris thickness distributions in these 5 zones are plotted in Fig. B2.

2. We divide the debris thickness into N_d bands, denoted by $d_j, \ j = 1, \ldots, N_d$. We define $\Delta d_j \equiv d_{j+1} - d_j$.

3. We estimate the area in the lth zone which has a debris thickness in the jth band, A_j^l, to be the fraction of the debris thickness observations in the lth zone that were in the jth band multiplied by the area of the lth zone.

Equation (2) in the main text gives the expression for the average ablation rate estimated using method II. It can be written as,

$$b_{II} = \frac{1}{A} \sum_{j=1}^{N_e} A_j^d \, \bar{b}_d(d_j) \tag{A6}$$

$$\bar{b}_d(d_j) = \frac{1}{T} \sum_{i=1}^{N_t} b_z(d_j, t_i) \Delta t_i \tag{A7}$$

$$A_j^d = \sum_{l=1}^{5} A_j^l \tag{A8}$$

640   The uncertainty in b_{II} is computed using the the following algorithm:

641   For $n = 1 - 1000$

642 1. Compute the parameters, b_{0in}, d_{0in} by fitting the data, $b^{obs}(d_m, t_i) + \Delta b^{obs}(d_m, t_i)$ to the function, $b_d(d)$,

643   given in equation (1) of the main text. Where $b^{obs}(d_m, t_i)$ is the observed ablation at the mth stake

644   with debris thickness d_m during the ith time period and $\Delta b^{obs}(d_m, t_i)$ is a Gaussian noise with standard

645   deviation $4\ cm$.

2. Compute the RMSD at each time period,

$$\Delta b_{dn}(t_i) = \sqrt{\frac{1}{N_d} \sum_m \left(b_{dn}(d_m, t_i) - b^{obs}(d_m, t_i)\right)^2} \tag{A9}$$

3. Compute the average RMSD over all the time periods,

$$\Delta \bar{b}_{dn} = \sqrt{\frac{1}{N_t} \sum_i \left(\Delta b_{dn}(t_i)\right)^2} \tag{A10}$$

4. Compute the net average ablation rate, b_{IIn},

$$b_{IIn} = \frac{\left(\sum_{j=1}^{N_d} \sum_{l=1}^{5} \left(A_j^l + \Delta A_{jn}^l\right)\right)\left(\bar{b}_{dn}(d_j) + \Delta \bar{b}_{dn}(d_j)\right)}{\sum_{j=1}^{N_d} \sum_{l=1}^{5} \left(A_j^l + \Delta A_{jn}^l\right)} \tag{A11}$$

646   where A_j^l is the estimated area of the jth debris thickness band in the lth zone., ΔA_{jn}^l is a Gaussian

647   noise with standard deviation equal to $0.3A_j^l$ and $\Delta \bar{b}_{dn}(d_j)$ is a Gaussian noise with standard deviation

648   equal to $\Delta \bar{b}_{dn}$

649 **APPENDIX B. SUPPLEMENTARY FIGURES**

650 The supplementary figures related to the computation of mass balance with method-I and method-II are

651 given below.

Fig. B1. Field photos of sub-debris ablation measurements at different stakes.
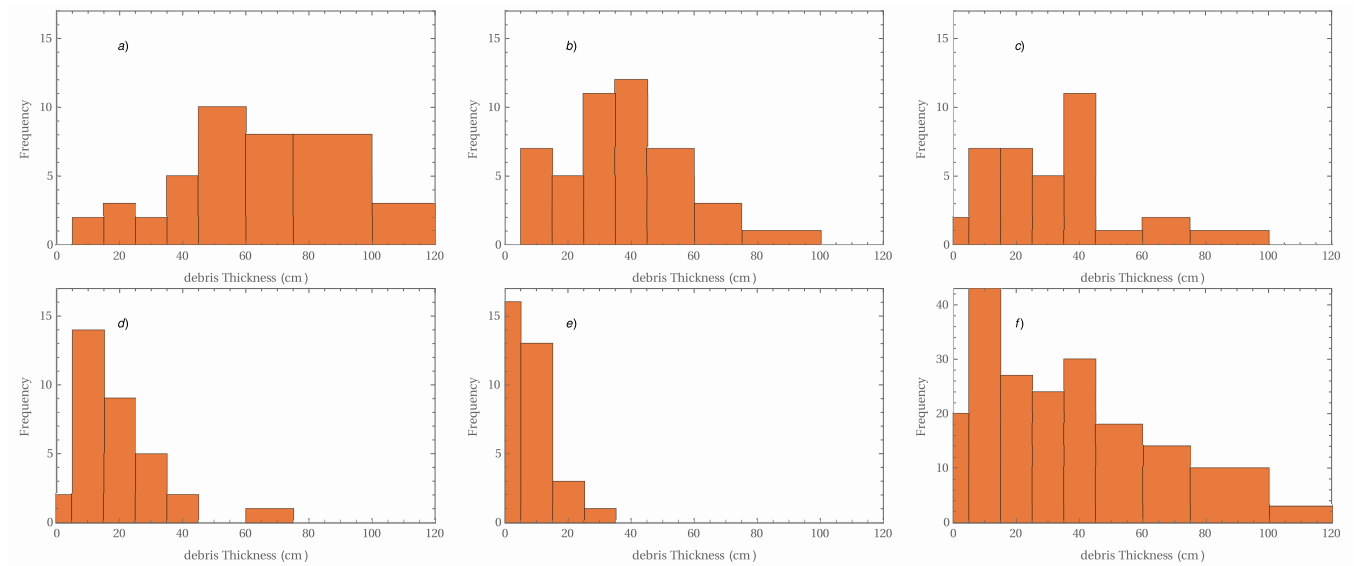
Fig. B2. (a-e)The frequency distribution of debris thickness for the five subzones defined in Fig.1. (f) The frequency distribution of all the measurements of debris thickness put together. Note the variable binsizes in these plots, and the different vertical range in sub-figure (f). Please see text for more details.
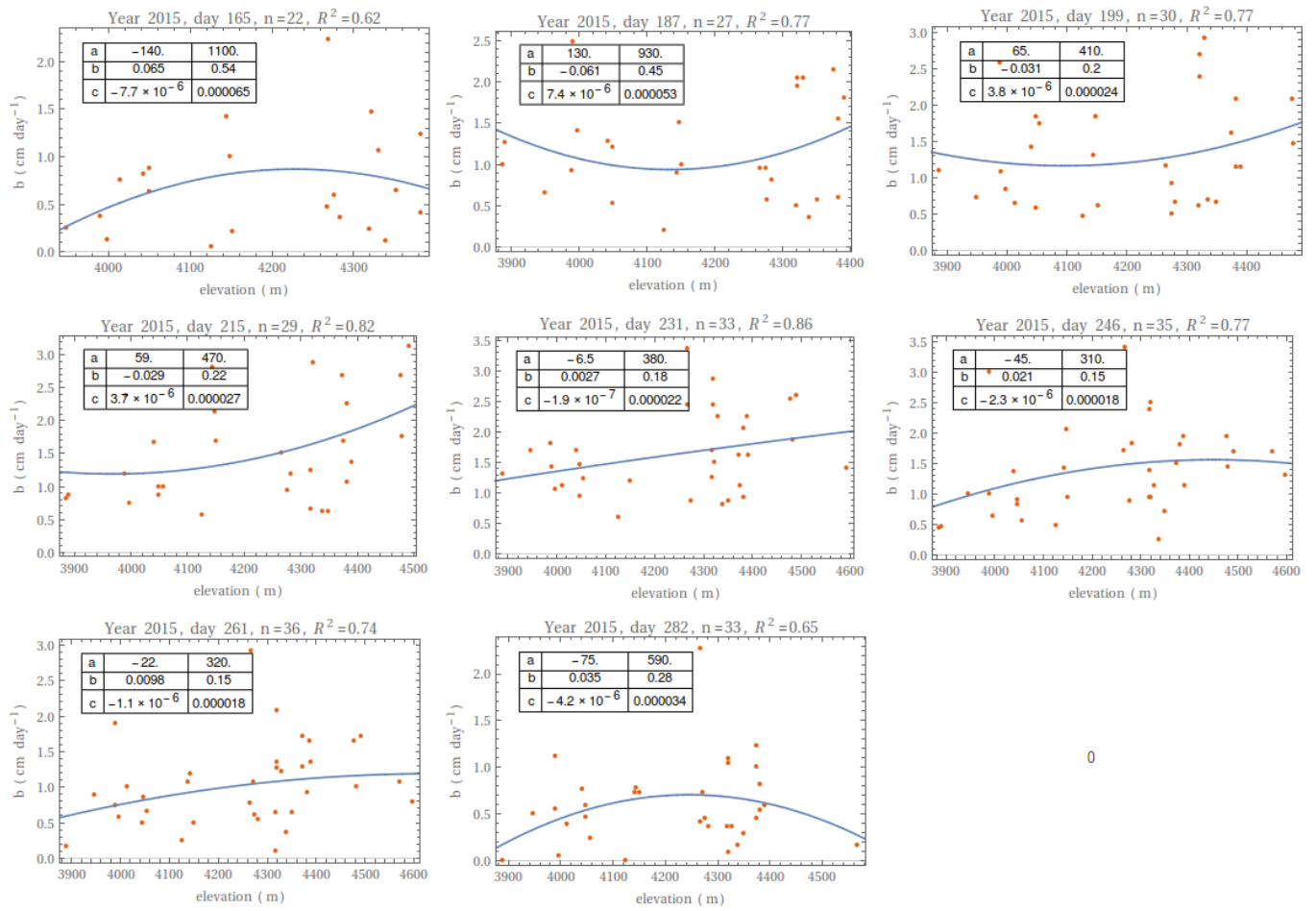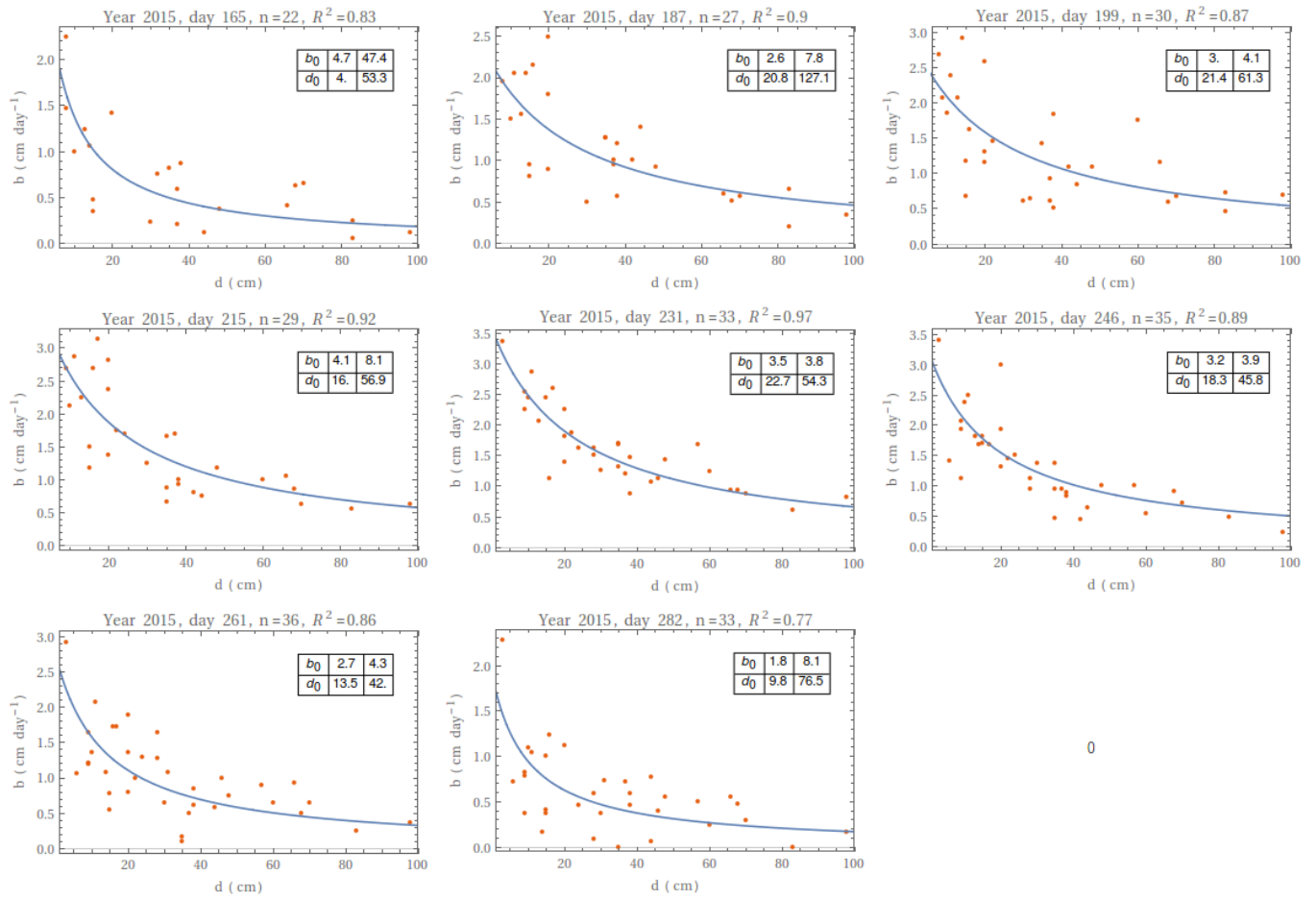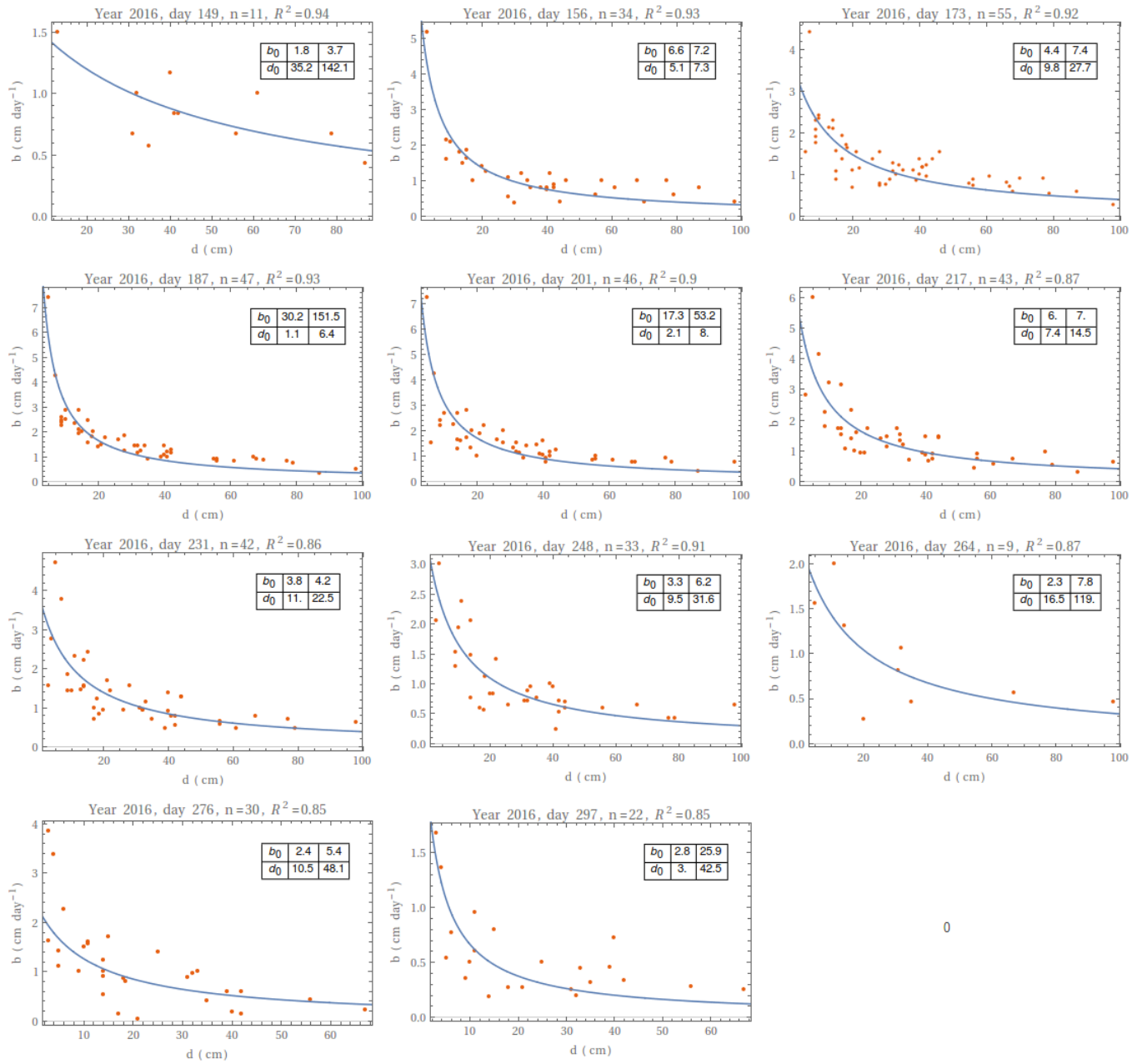
Fig. B3. The fitted $b_z(z)$ for the all the ablation rate data from the debris-covered ablation zone in 2015 for each of the observation periods. The fit parameters are given in inset along with corresponding uncertainties.
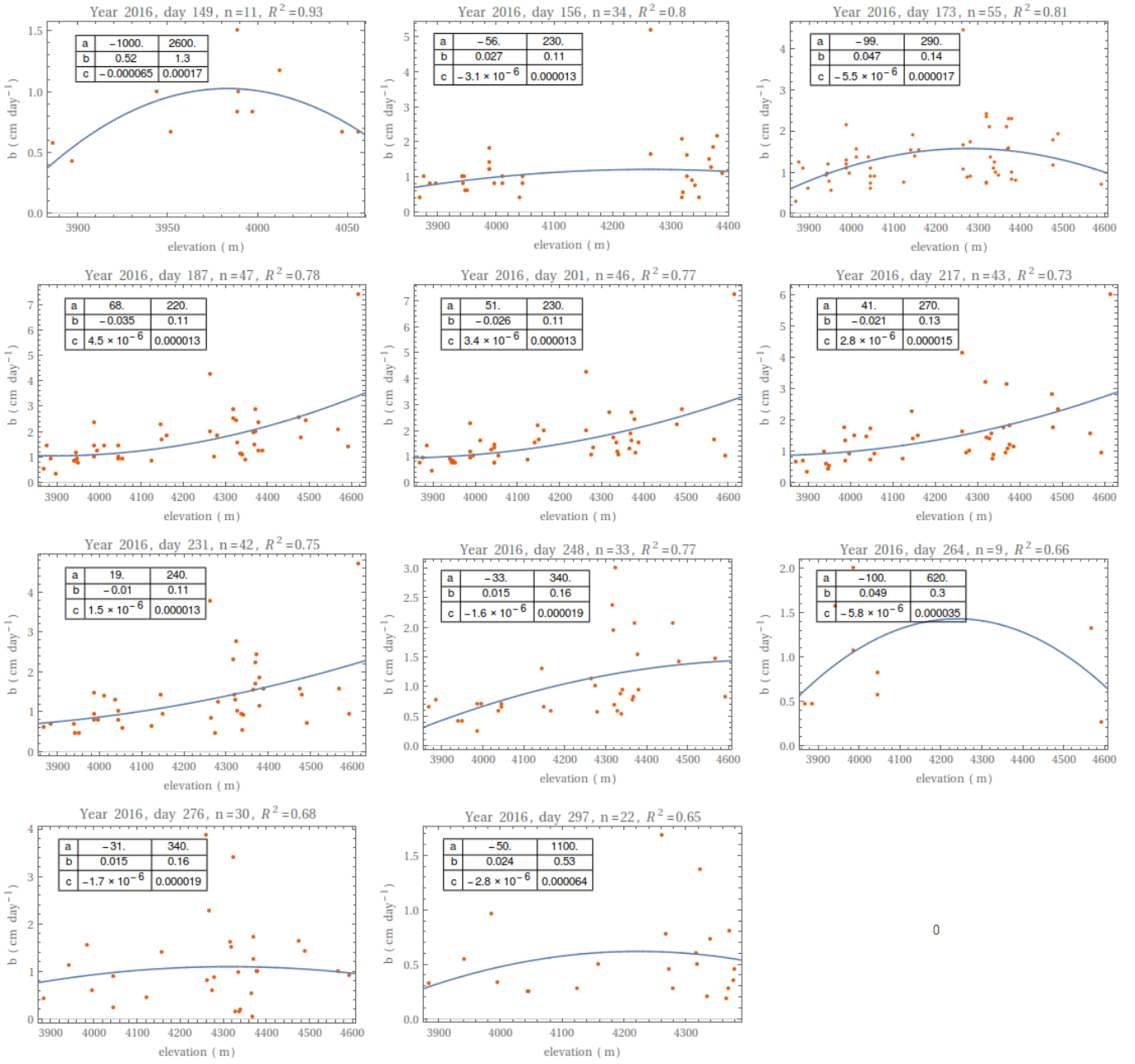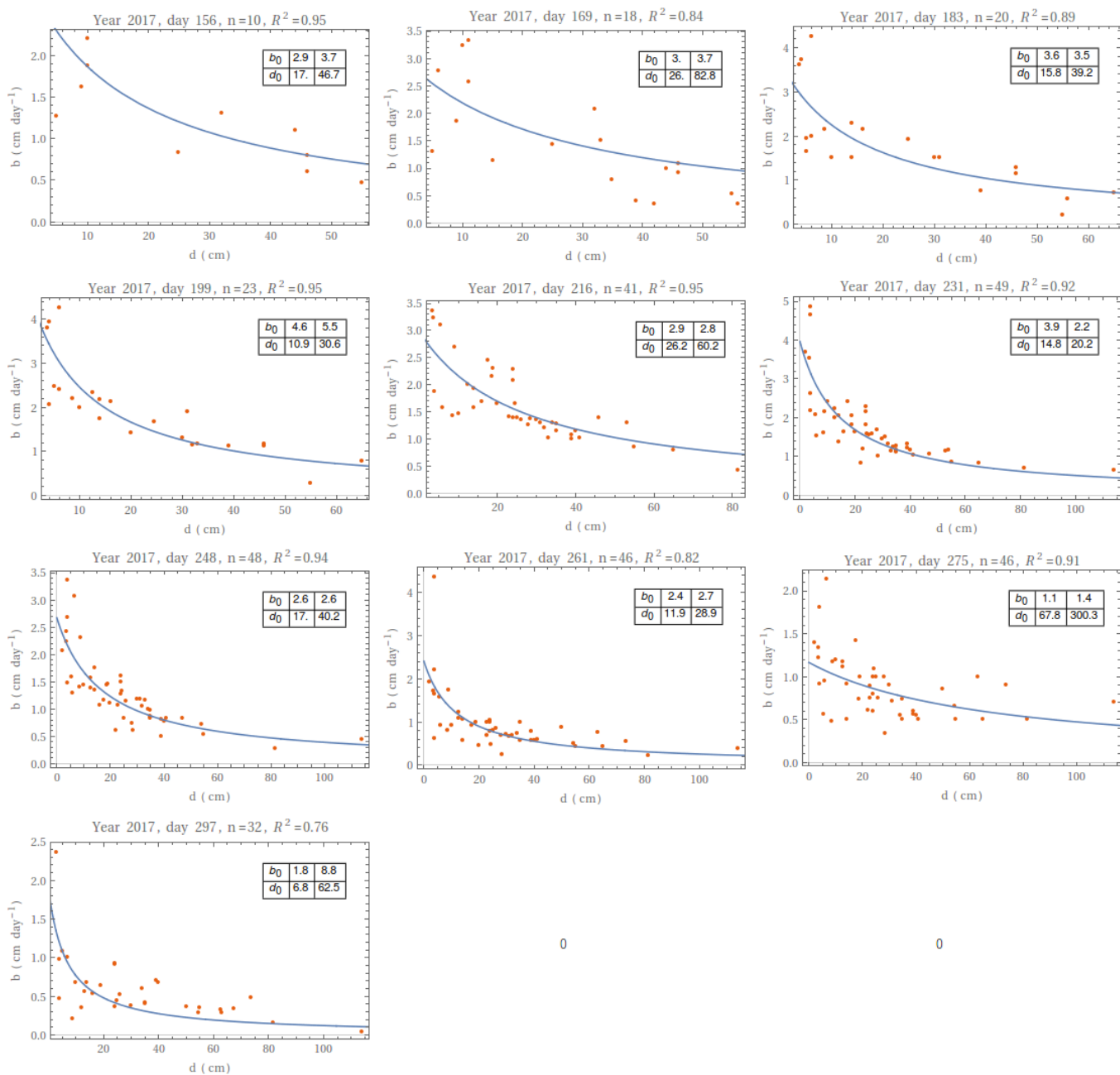
Fig. B4. The fitted $b_z(z)$ for the all the ablation rate data from the debris-covered ablation zone in 2016 for each of the observation periods. The fit parameters are given in inset along with corresponding uncertainties.
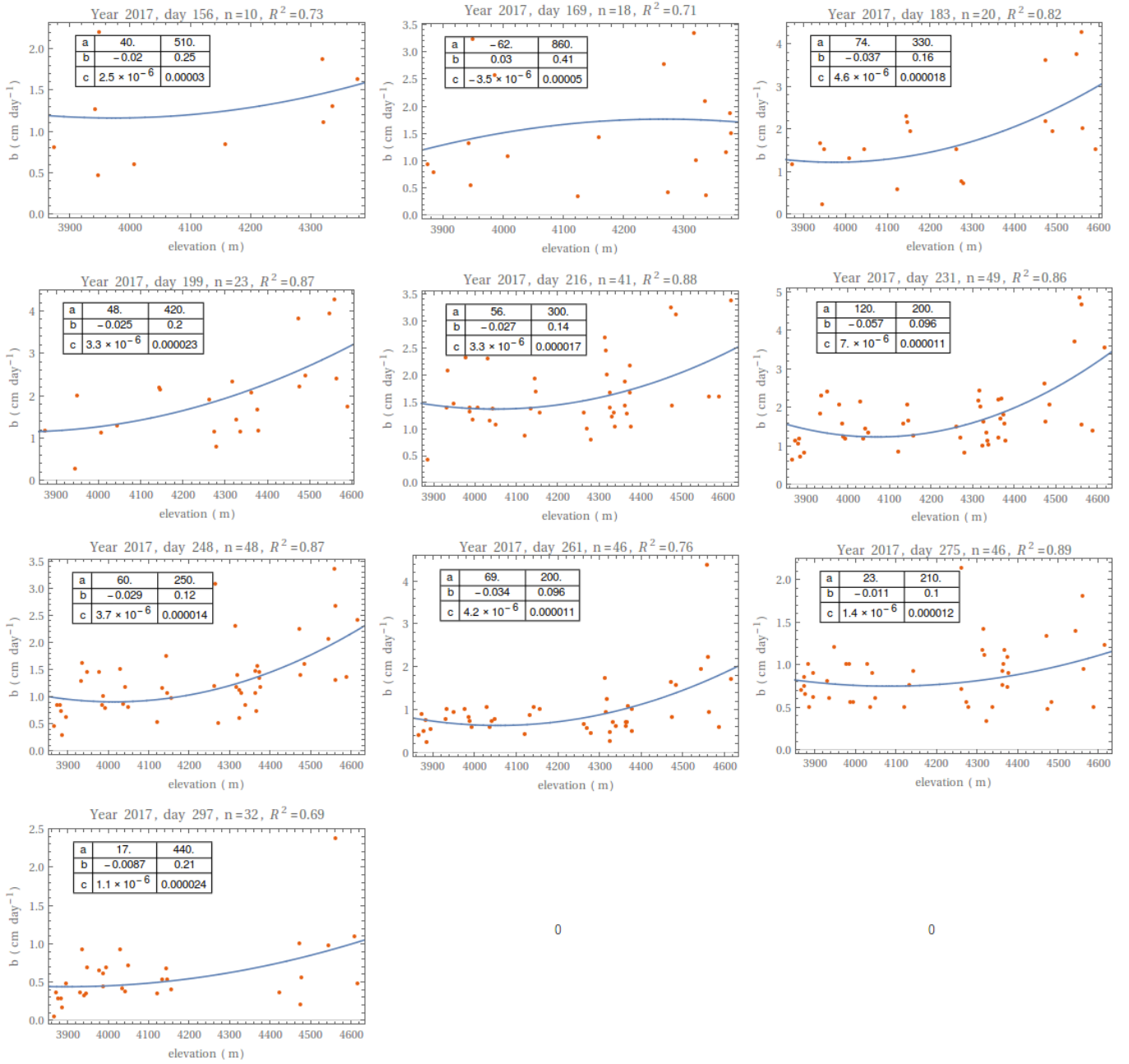
Fig. B5. The fitted $b_z(z)$ for the all the ablation rate data from the debris-covered ablation zone in 2017 for each of the observation periods. The fit parameters are given in inset along with corresponding uncertainties.

Fig. B6. The fitted $b_d(d)$ for the all the ablation rate data from the debris-covered ablation zone in 2015 for each of the observation periods. The fit parameters are given in inset along with corresponding uncertainties.

Fig. B7. The fitted $b_d(d)$ for the all the ablation rate data from the debris-covered ablation zone in 2016 for each of the observation periods. The fit parameters are given in inset along with corresponding uncertainties.

Fig. B8. The fitted $b_d(d)$ for the all the ablation rate data from the debris-covered ablation zone in 2017 for each of the observation periods. The fit parameters are given in inset along with corresponding uncertainties.
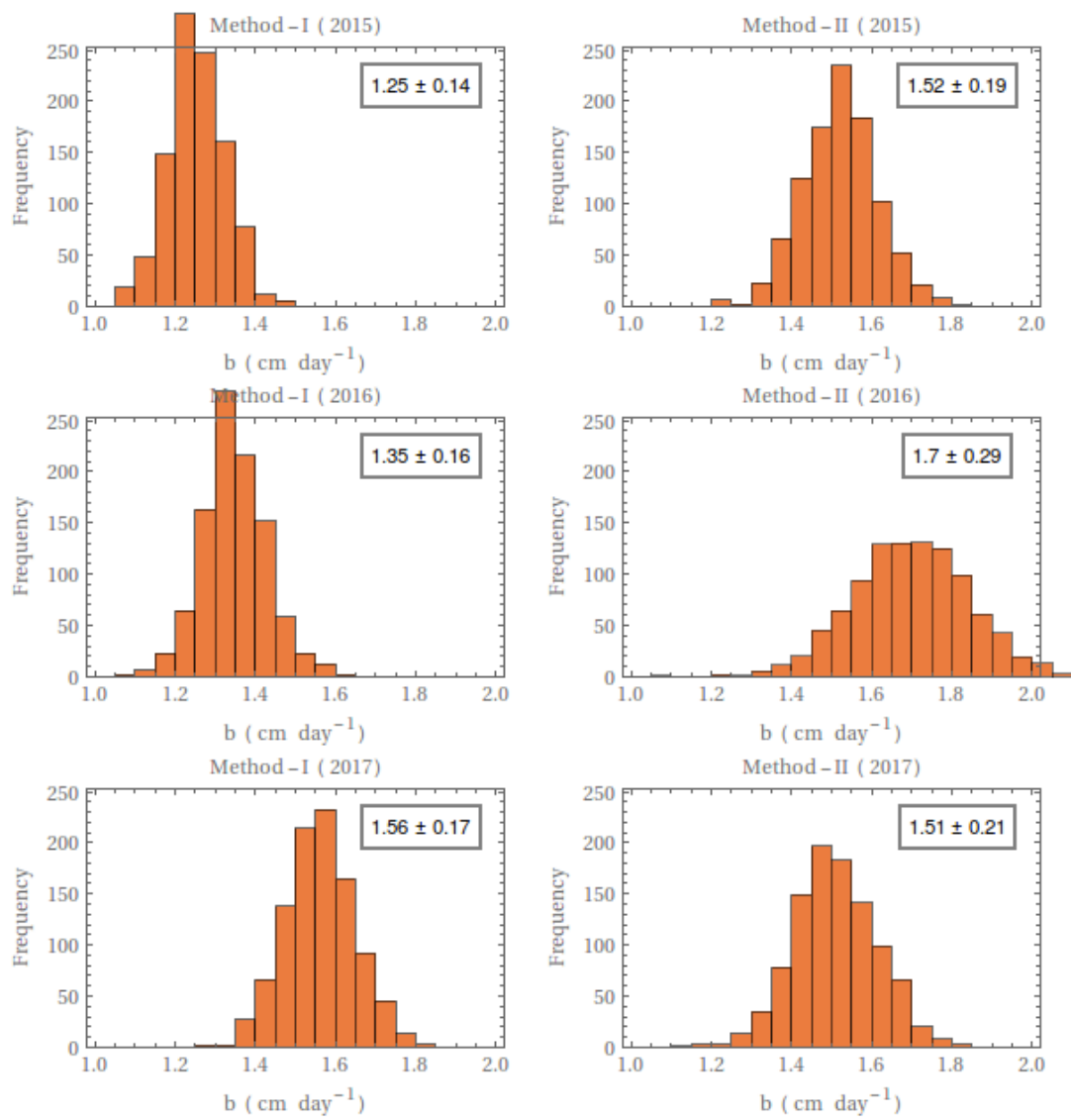
Fig. B9. The distribution of mean specific ablation rate over the debris-covered ablation zone generated in the Monte Carlo simulations for method-I and method-II. The mean and 2σ error bars are given in insets.
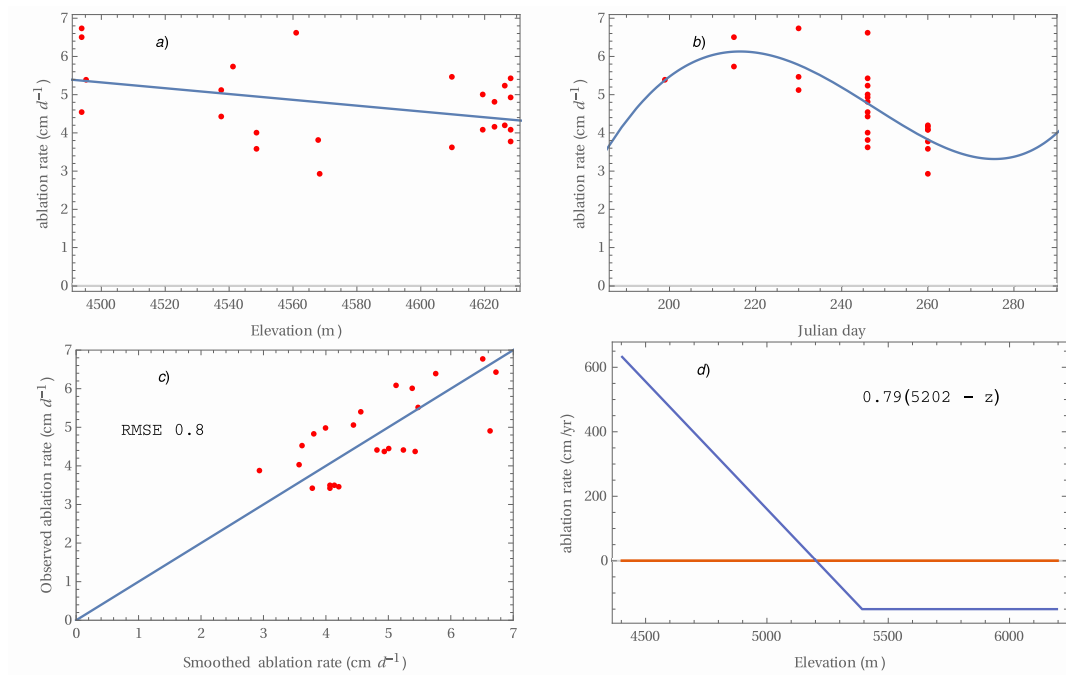
Fig. B10. The clean-ice ablation rate observations (red solid circles) in the melt season of 2015 as a function of a) elevation and b) Julian day. The blue solid line denote the corresponding fitted form $b_1(z)$ and $b_2(t)$ as described in the text. c) A comparison of smoothed and observed clean ice ablation rate with RMSE of the fit given in cm d^{-1}. d) The annual smoothed mass balance profile (solid blue line) for the clean part of the glacier. See text for more details.
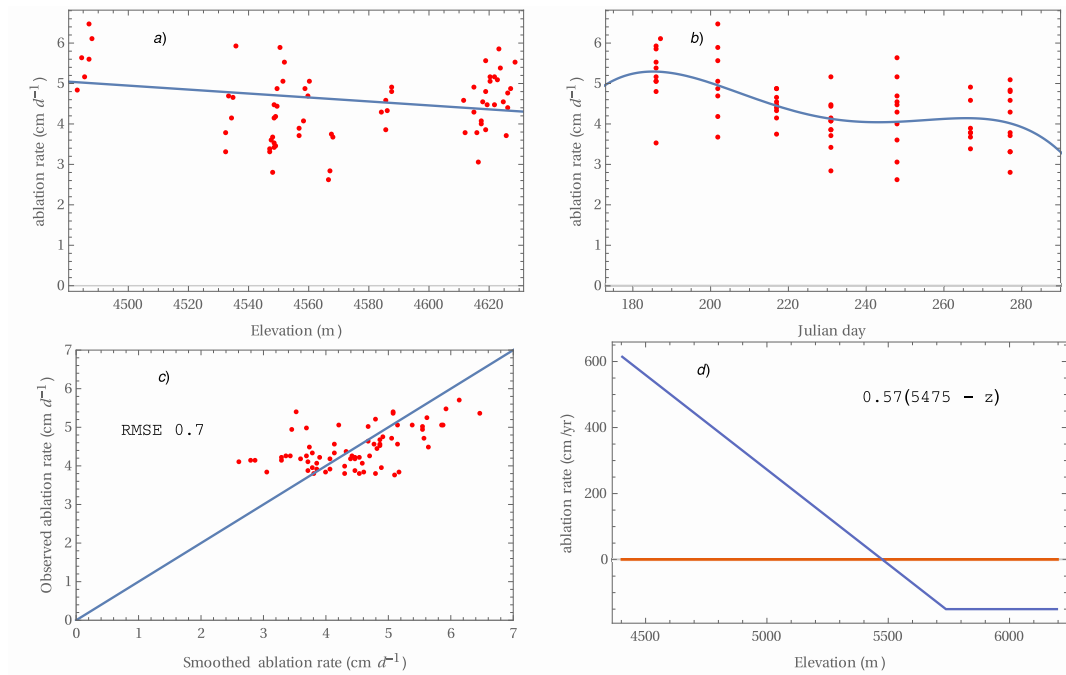
Fig. B11. The clean-ice ablation rate observations (red solid circles) in the melt season of 2016 as a function of a) elevation and b) Julian day. The blue solid line denote the corresponding fitted form $b_1(z)$ and $b_2(t)$ as described in the text. c) A comparison of smoothed and observed clean ice ablation rate with RMSE of the fit given in cm d^{-1}. d) The annual smoothed mass balance profile (solid blue line) for the clean part of the glacier. See text for more details.
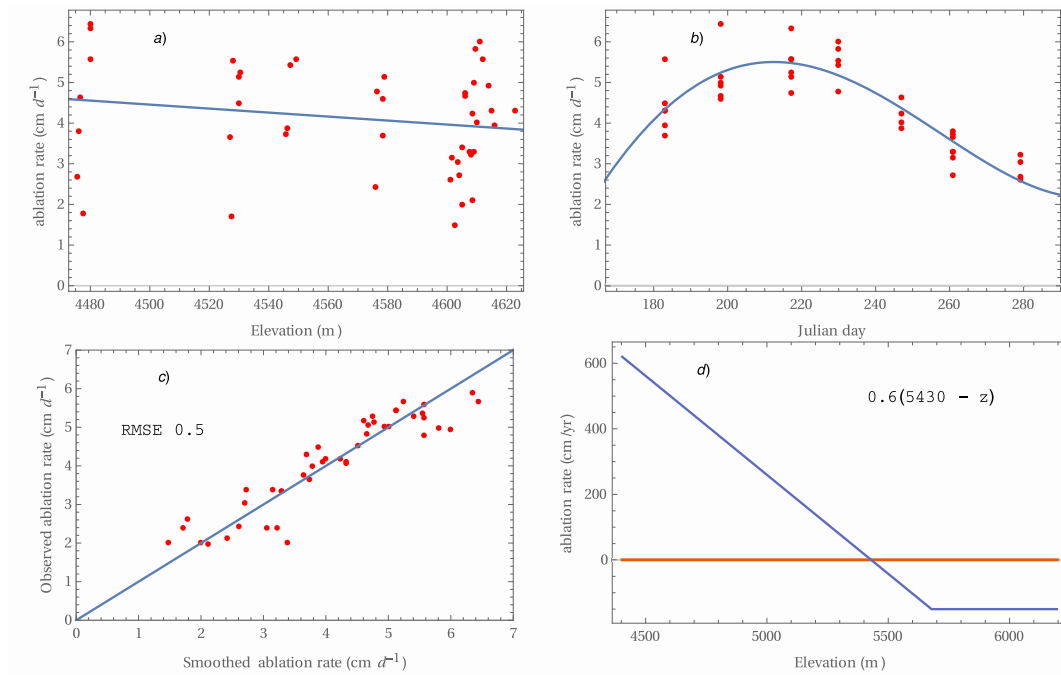
Fig. B12. The clean-ice ablation rate observations (red solid circles) in the melt season of 2017 as a function of a) elevation and b) Julian day. The blue solid line denote the corresponding fitted form $b_1(z)$ and $b_2(t)$ as described in the text. c) A comparison of smoothed and observed clean ice ablation rate with RMSE of the fit given in cm d^{-1}. d) The annual smoothed mass balance profile (solid blue line) for the clean part of the glacier. See text for more details.
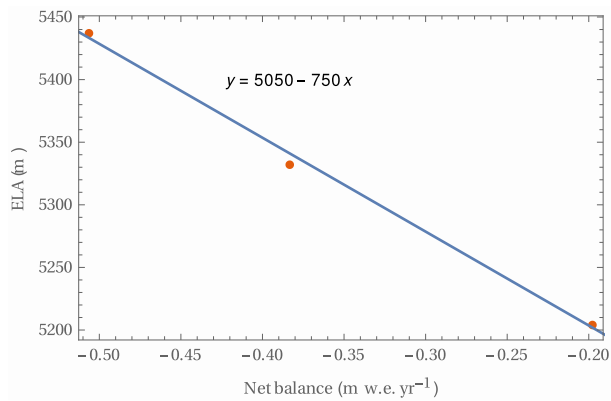
Fig. B13. The estimates of ELA of Satopanth Glacier (solid symbol) for 2015, 2016, and 2017 showed an linear behaviour (best-fit straight line shown with solid line) as a function of annual net specific balance.